Available online at www.sciencedirect.com

ScienceDirect

Geochimica et Cosmochimica Acta 239 (2018) 390–408

Geochimica et Cosmochimica Acta

www.elsevier.com/locate/gca

Formation of abiotic hydrocarbon from reduction of carbonate in subduction zones: Constraints from petrological observation and experimental simulation

Renbiao Tao [a], Lifei Zhang [a,*], Meng Tian [a], Jianjiang Zhu [a], Xi Liu [a], Jinzhong Liu [b], Heidi E. Höfer [c], Vincenzo Stagno [d], Yingwei Fei [a,e]

[a] *The MOE Key Laboratory of Orogenic Belt and Crustal Evolution, School of Earth and Space Sciences, Peking University, Beijing 100871, China*

[b] *State Key Laboratory of Organic Geochemistry, Guangzhou Institute of Geochemistry, Chinese Academy of Sciences, Guangzhou 510640, China*

[c] *Institut für Geowissenschaften, Mineralogie, Goethe-Universität, 60438 Frankfurt am Main, Germany*

[d] *Department of Earth Sciences, Sapienza University of Rome, Rome 00185, Italy*

[e] *Geophysical Laboratory, Carnegie Institution of Washington, Washington, DC 20015, USA*

Received 11 December 2017; accepted in revised form 3 August 2018; Available online 12 August 2018

Abstract

Subduction is a key process for linking the carbon cycle between the Earth's surface and its interior. Knowing the carbonation and decarbonation processes in the subduction zone is essential for understanding the global deep carbon cycle. In particular, the potential role of hydrocarbon fluids in subduction zones is not well understood and has long been debated. Here we report graphite and light hydrocarbon-bearing inclusions in the carbonated eclogite from the Southwest (S.W.) Tianshan subduction zone, which is estimated to have originated at a depth of at least 80 kilometers. The formation of graphite and light hydrocarbon likely results from the reduction of carbonate under low oxygen fugacity (~FMQ - 2.5 log units). To better understand the origin of light hydrocarbons, we also investigated the reaction between iron-bearing carbonate and water under conditions relevant to subduction zone environments using large-volume high-pressure apparatus. Our high-pressure experiments provide additional constraints on the formation of abiotic hydrocarbons and graphite/diamond from carbonate-water reduction. In the experimental products, the speciation and concentration of the light hydrocarbons including methane (CH_4), ethane (C_2H_6), and propane (C_3H_8) were unambiguously determined using gas chromatograph techniques. The formation of these hydrocarbons is accompanied by the formation of graphite and oxidized iron in the form of magnetite (Fe_3O_4). We observed the identical mineral assemblage (iron-bearing dolomite, magnetite, and graphite) associated with the formation of the hydrocarbons in both naturally carbonated eclogite and the experimental run products, pointing toward the same formation mechanism. The reduction of the carbonates under low oxygen fugacity is, thus, an important mechanism in forming abiotic hydrocarbons and graphite/diamond in the subduction zone settings.

Keywords: Abiotic hydrocarbon; Graphite; Oxygen fugacity; Subduction zone; High-pressure experiments; S.W. Tianshan

1. INTRODUCTION

Subduction is considered as a factory for the recycling of elements such as carbon between the Earth's interior and

* Corresponding author.
E-mail address: Lfzhang@pku.edu.cn (L. Zhang).

https://doi.org/10.1016/j.gca.2018.08.008
0016-7037/

surface (Hacker, 2003; Tatsumi, 2005). It plays a key role in the deep carbon cycle (Javoy et al., 1982; Dasgupta, 2013). Carbon is recycled into the Earth's interior via subduction of different carbon-bearing phases (e.g., carbonate), and it is partly released to the surface by metamorphism in the subduction zone and volcanism at islands arcs (Berner, 1999; Sleep and Zahnle, 2001). Therefore, knowing the behavior of the carbon-bearing phases in the subduction zone is of particular interest for understanding the global deep carbon cycle (Ague and Nicolescu, 2014; Kelemen and Manning, 2015; Poli, 2015; Duncan and Dasgupta, 2017).

Most of the previous studies on the stability of the carbon-bearing phases at the subduction condition focused on the variables of pressure and temperature (Isshiki et al., 2004; Poli et al., 2009). In fact, the redox conditions also control the speciation and stability of carbon-bearing phases during subduction, which ~~is~~ are still poorly explored (Connolly, 1995; Galvez et al., 2013). Taken a carbon-saturated C—O—H fluid as an example, the ratio of CH_4 and CO_2 varies with the redox condition of the system (Connolly, 1995). Therefore, defining the oxygen fugacity (fO_2) of the subducting slab is necessary in order to discuss the stability of different carbon forms (e.g. graphite and hydrocarbons). In the subduction zone, the speciation, mobility, and residence time of the carbon phases are strongly coupled to fO_2 (Bryndzia and Wood, 1990; Luth, 1993; Stagno et al., 2015). Thermodynamics predictions of the redox profile of the subducting slab show that at oxidizing conditions at depth of 100 km ($fO_2 > \sim$FMQ - 1, i.e., 1 log unit below the fayalite-magnetite-quartz oxygen fugacity buffer) the mobile species, such as CO_2 fluid or carbonatite melt, are stable; at relatively low fO_2 ($fO_2 < \sim$FMQ - 1), the immobile carbon species, diamond or graphite, are stable; while at extremely reduced conditions ($< \sim$FMQ - 3), the carbon species within the C—O—H fluid system are mobile again as hydrocarbon-rich fluid (Frost, 1979; Matveev et al., 1997; Frost, 2012; Stagno et al., 2015). Carbon can enter subduction zones in the form of minor biotic organic matter, sedimentary carbonate, and altered carbonates in the crust (Staudigel et al., 1989; Alt and Teagle, 1999; Plank, 2014). The most biotic organic matter may decompose or be exhausted by metamorphic reaction with oxidized matter (e.g. Fe—Mn oxides) before subduction proceeds (Claypool and Kaplan, 1974; Froelich et al., 1979). The stability of polymerized fluids, indeed, has been reported in literature either from evidences in natural rocks (Frezzotti et al., 2011), or by thermodynamic calculations that take into account the solubility behavior of silicate minerals in water-rich fluids at mantle conditions (Sverjensky et al., 2014) as a function of pressure, temperature and oxygen fugacity. Further theoretical predictions and experimental simulations showed these hydrocarbon fluids are immiscible in the subduction environments (Huang et al., 2017; Li, 2016). However, to date, limited natural observations were confirmed for the formation of abiotic hydrocarbons in the subduction environments.

The formation of the abiotic hydrocarbons in nature provides a unique window into our understanding of organic-inorganic interactions. It is well documented that most known natural hydrocarbons are of biogenic origin. However, there are several recent reports that have demonstrated that some hydrocarbons, particularly methane and other light hydrocarbons, were derived from abiotic precursors in various geological settings related to deep processes (Etiope and Schoell, 2014, and references therein). Abiotic alkanes have been found in the Earth's lower crust (Lollar et al., 2002) and the Precambrian Shields (Lollar et al., 2008). Abundant abiotic methane (CH_4) has also been found in orogenic harzburgite rocks of the Early Paleozoic suture zone in northwestern China (Song et al., 2009), and in natural diamonds from Congo and Brazil (Melton and Giardini, 1974). More intriguingly, hydrocarbon-bearing fluid inclusions have been widely observed in metamorphic rocks from subduction zones, such as the Dabie-Sulu terranes in eastern China, the jadeite tract in Myanmar, the Sanbagawa belt in Japan, the Raspas Complex in Ecuador, and Alps belts in Italy (Fu et al., 2003; Shi et al., 2005; Arai et al., 2012; Herms et al., 2012; Brovarone et al., 2017). For these hydrocarbons observed in metamorphic rocks from subduction zones, it is still hard to distinguish whether they are abiotic or not, because normally only tiny amounts of hydrocarbons are trapped as fluid inclusions in metamorphic minerals.

Here, we report the presence of light hydrocarbon-bearing fluid inclusions and graphite in the carbonated eclogites from the S.W. Tianshan UHP oceanic subduction zone. The observed light hydrocarbon-bearing inclusions and graphite likely results from an abiotic reduction of Fe-bearing carbonate and metamorphic fluids, supported by the low oxygen fugacity constrained by the coexisting minerals. Furthermore, high-pressure experiments in the system containing iron-bearing dolomite (ankerite) and water were carried out to provide additional support for the formation of abiotic light hydrocarbons from carbonate reduction under subduction settings.

2. GEOLOGICAL SETTING AND SAMPLE DESCRIPTIONS

2.1. Geological setting

Composed of marble, metapelite, blueschist, eclogite, and serpentinite, the Chinese Tianshan orogenic belt extends for more than 200 km between the Tarim plate and the Yili-central Tianshan plate (Fig. 1). It is the world largest known oceanic (U)HP metamorphic orogen, confirmed by quartz exsolution lamellae in omphacite (Zhang et al., 2002a), residual magnesite in dolomite in eclogite (Zhang et al., 2002b), coesite in the eclogite and metapelite (Lü et al., 2008; Yang et al., 2013), decomposition structure of dolomite in eclogite and metapelite (Zhang et al., 2007; Tao et al., 2014), and Ti-chondrodite- and Ti-clinohumite-bearing serpentinized ultramafic rocks (Shen et al., 2015). Maximum metamorphic pressure-temperature conditions are constrained to ~3 GPa and ~600 °C by phase equilibrium calculations and petrological occurrence of coesite (Lü et al., 2009; Tian and Wei, 2012). Metamorphic basalt with pillow structure and MORB/OIB-like geochemical characteristics indicates the S.W.

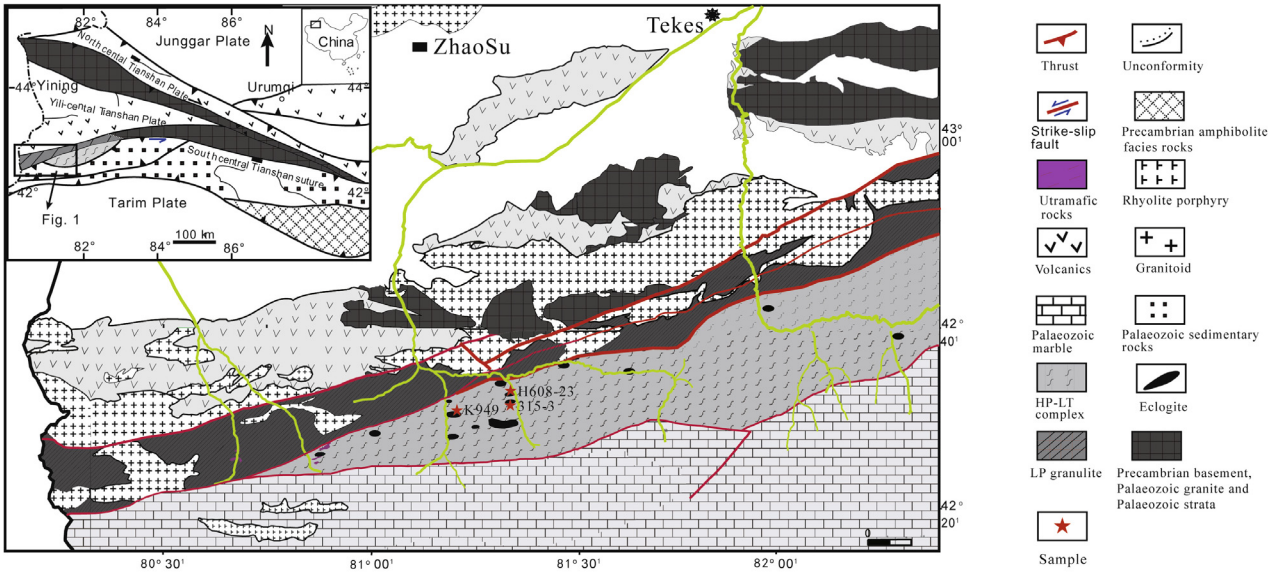

Fig. 1. (a) Geological map of the S.W. Tianshan UHP subduction metamorphic belt, western China, modified after (Lü et al., 2012). The red stars illustrate sample locations in this study. All three samples were collected in the same drainage area of the Habutengsu River. (For interpretation of the references to colour in this figure legend, the reader is referred to the web version of this article.)

Tianshan is a typical oceanic subduction orogenic belt (Ai et al., 2006; Xiao et al., 2012).

2.2. Sample descriptions

Carbonation (5–30 vol.%) is very common in most (U) HP meta-ophiolites (e.g. carbonated metapelite, carbonated eclogite and carbonated serpentinite) from the S.W. Tianshan subduction orogen (Zhang et al., 2002b, 2007; Lü et al., 2013; Li et al., 2014; Tao et al., 2014; Shen et al., 2015). Dotted graphites are dispersed in all kinds of meta-ophiolites (e.g., metapelite and marbles) from S.W. Tianshan subduction zones (Lü et al., 2013). These large amounts of carbon-bearing phases (e.g. carbonate and graphite) in different meta-ophiolite after (U)HP metamorphism from the S.W. Tianshan subduction belt is important sources of carbon recycled into the deep Earth, and it makes ideal samples for studying the deep carbon cycle in subduction zones (Tao et al., 2014). We have petrologically and geochemically characterized tens of carbonated eclogite samples from the S.W. Tianshan subduction zone in previous studies (Tao et al., 2014; Tao et al., 2018a). In this study, three carbonated eclogites (315-3, H608-23 and K949) were selected to investigate possible formation and preservation of abiotic hydrocarbons in the S.W. Tianshan subduction zone. Their locations are marked with red stars on the schematic geological map (Fig. 1). All three samples were collected in the same drainage areas of the Habutengsu River.

3. METHODS

3.1. Petrological analyses

Petrological studies are carried out on carbonated eclogites with optical microscopy, Raman spectroscopy, scanning electron microscopy (SEM), and electron probe microanalysis (EPMA). Raman spectra from 100 to 1600 cm^{-1} were collected on carbon-bearing phases (carbonates, graphite, and fluid inclusions) in carbonated eclogites at ambient condition by using a confocal micro-Raman spectroscopy (Renishaw system RM-1000; 514.5 nm Ar-ion laser operating at 20 mW; back-scattering geometry; 60 s counting time). Backscatter Electron (BSE) images were collected on thin sections without carbon coating by using an FE-SEM (Quanta 650 FEG; low vacuum mode and 15 kV), and chemical compositions of the mineral phases in the carbonated eclogites were determined with carbon-coated thin sections by using a JEOL JXA-8900R electron microprobe. Synthetic silica (Si) and spessartine (Mn), natural pyrope (Mg, Al), andradite (Fe, Ca), albite (Na), rutile (Ti) and sanidine (K) were used as standards. A ZAF correction program was used to reduce final results. The bulk compositions of the carbonated eclogites were obtained by X-ray fluorescence (XRF). All petrological analyses in this study were conducted at the MOE Key Laboratory of Orogenic Belt and Crustal Evolution at Peking University.

3.2. Measurement of Fe^{3+} in garnet using the "Flank method

Garnets containing both Fe^{3+} and Fe^{2+} are potentially sensors of fO_2 in metamorphic rocks from subduction zones and in garnet peridotite from the mantle (Luth et al., 1990; Woodland and O'Neill, 1993; Stagno et al. 2013; Stagno et al., 2015). To constrain the oxygen fugacity of the S.W. Tianshan subduction zone, the Fe^{3+} concentrations in eclogitic garnet were measured by the "Flank method" with the electron microprobe (Höfer and Brey, 2007). The $Fe^{3+}/\Sigma Fe$ ratio profile of garnet in carbonated eclogite (K949) was measured from core to rim by the "Flank method" at the microprobe laboratory of Institut für Geowissenschaften, Mineralogie, Goethe-Universität, where the "Flank

method" was developed (Höfer et al., 1994). Höfer and Brey (2007) determined the iron oxidation state of garnet with the "Flank method" and yielded as precise and accurate results as Mössbauer spectroscopy. For this study, the "Flank method" was calibrated on a JEOL JXA 8900RL microprobe. The FeLα and Lβ intensities were measured for a fixed counting time of 300 s each at 15 kV and 200 nA. The iron metal Lα line was used to optimize the PHA conditions (in differential mode) for the measurement of FeLα and Lβ intensity. One spectrometer with a TAP crystal and smallest detector slit (300 μm) were used for the "Flank method" measurements. The remaining 4 spectrometers simultaneously carried out quantitative analyses of 12 elements (Si, Ti, Al, Cr, Fe, Mn, Ni, Mg, Ca, Na, K, P) with appropriate standards, e.g., pyrope (Mg, Si), almandine (Fe), $MnTiO_3$ (Mn, Ti), $CaSiO_3$ (Ca), and garnets with variable total Fe and $Fe^{3+}/\Sigma Fe$ known from Mössbauer "milliprobe" (McCammon et al., 1991). The garnet $Fe^{3+}/\Sigma Fe$ ratio was determined with the "Flank method" by correcting for self-absorption. The detailed procedure of the "Flank method" measurement of the $Fe^{3+}/\Sigma Fe$ ratio in garnets is described in the publication by Höfer and Brey (2007) and Tao et al. (2018b). In order to increase the intensity of the FeLα and Lβ emission and for a better statistically based precision, we used the higher probe current of 200 nA in this study compared to the first calibration of the "Flank method" by Höfer and Brey (2007). In addition, the major chemical compositions (e.g. Si, Ti, Al, Cr, Fe, Mn, Ni, Mg, Ca, Na, K) of the garnets and their inclusions (e.g. omphacite) were analyzed by EPMA to be able to calculate the oxygen fugacity conditions of carbonated eclogites from the S.W. Tianshan subduction zone using the garnet-clinopyroxene oxybarometer (Stagno et al., 2015).

3.3. Thermodynamical constraint of P-T-fo_2 evolution

Thermodynamic phase equilibrium modeling is a common method for reconstructing PT condition of metamorphic rocks. In this study, we calculated pressure and temperature conditions of carbonated eclogite (K949) from S.W. Tianshan subduction zone by phase equilibria modelling in the system of MnO - Na_2O - CaO - K_2O - FeO - MgO - Al_2O_3 - SiO_2 - H_2O - O - CO_2 (MnNCKFMASHO-CO_2) considering the mineral assemblages and bulk compositions. The bulk-rock chemical compositions of carbonated eclogite (K949) for pseudosection calculation was normalized in the MnNCKFMASHO system. Quartz/coesite is considered in excess because ubiquitous quartz was observed in the thin section. TiO_2 and P_2O_5 are neglected as they are mainly present as rutile/ilmenite and apatite accessory phases. 5 wt% of carbonate (similar to optical observation) was included in the system as representative of the stability of carbon-bearing phases in the carbonated eclogites. The molar amount of $CO_2 + H_2O$ was set to be in excess, which is consistent with fluid-saturated conditions in the cold subduction zones (Okamoto and Maruyama, 1999). P-T pseudosections were calculated using the software THERMOCALC 3.33 (Holland and Powell, 1998) with the updated version of the dataset (Holland and Powell, 1998). Activity-composition relationships of metamorphic minerals (e.g. garnet, omphacite) are taken as in a previous study (Tian and Wei, 2012). Lawsonite, aragonite, calcite and quartz/coesite were treated as pure end-member phases. The chemical composition profile of garnets from the carbonated eclogite (K949) was plotted on the isopleths of garnet end-members in the pseudo-section phase diagram to constrain the P-T evolution trend of S.W. Tianshan subduction zone.

The redox chemical equilibrium, $5CaFeSi_2O_6$ (hedenbergite) + $1/3Ca_3Al_2Si_3O_{12}$ (grossular) + $O_2 = 2Ca_3Fe_2Si_3O_{12}$ (andradite) + $1/3Fe_3Al_2Si_3O_{12}$ (almandine) + $4SiO_2$ (coesite) (Stagno et al., 2015) was used that requires the knowledge of Fe^{3+} content of garnet to calculate the fO_2 evolution of carbonated eclogite (K949). The thermodynamic data used for the equation are from Holland and Powell (2011). The activity-composition relations for garnet solid solution were modified from Gudmundsson and Wood (1995). The Fe^{3+} content of the garnets from the "Flank method" was used to calculate the activity of grossular ($Ca_3Al_2Si_3O_{12}$), almandine ($Fe_3Al_2Si_3O_{12}$) and andradite ($Ca_3Fe_2Si_3O_{12}$) end-members of garnet. The oxygen fugacity evolution trend of carbonated eclogite (K949) was constrained by the paired garnet host and omphacite inclusion formed at different metamorphic stages.

The fO_2 of carbonated eclogite (H608-23) was also thermodynamically constrained by the coexisting ankerite, calcite, magnetite, and graphite assemblages in the CaO-FeO-H_2O-CO_2 system. The pressure-fO_2 phase diagram was thermodynamically calculated in the CaO-FeO-CO_2-O system at 550 °C to constrain the fO_2 at which Fe-bearing carbonate (ankerite) was reduced to magnetite and graphite using the ThermoCalc program with the improved thermodynamic dataset (Holland and Powell, 2011).

3.4. High-pressure experiment simulation

In order to further explore the abiotic formation of hydrocarbon-bearing fluid inclusions and graphite in the carbonated eclogite, we have designed and conducted a series of experiments on the reaction of Fe-bearing dolomite (ankerite) plus water under typical pressure-temperature conditions of subduction zones and upper mantle. Previous experiments have focused on the formation of graphite and light hydrocarbon fluid from carbonate reduction at relatively low pressures at MPa ranges (e.g., Giardini and Salotti, 1969; McCollom, 2003; Milesi et al., 2015). In this study, we have extended these experiments to pressures between 1 and 6 GPa at temperatures of 600–1200 °C using a piston-cylinder apparatus and a large cubic press.

3.4.1. Experimental conditions

Natural ankerite was used as starting material. Its chemical composition, $Ca_{1.02}(Fe_{0.52}Mg_{0.43}Mn_{0.04})(CO_3)_2$, was confirmed with a JXA-8900 microprobe at the Geophysical Laboratory (Carnegie Institution of Washington). For the high-pressure experiments, two different diameters of gold capsules were used, 2.5 mm and 5 mm in diameter respectively. Beforehand, the capsule was crimped, sealed at one

end by arc welding, boiled twice in diluted HCl (30 min at 250 °C), and ultrasonically cleaned in distilled water (20 min) to thoroughly remove possible organic matter. We first loaded ~10 weight % distilled water to the bottom of the capsule, and then loaded the ankerite powder, that means the water/rock weight ratio is ~1:9. The loaded capsule, surrounded by wet tissue, was quickly sealed by arc welding.

High-pressure experiments were carried out at the High-Pressure and High-Temperature Laboratory, Peking University (PKU) (Liu et al., 2012a; Tao et al., 2017a). Experiments below 2 GPa were carried out using the Quick Press piston-cylinder apparatus, while experiments above 3 GPa were performed using a CS-IV 6×14 MN cubic press. Details of the cell assemblies and calibrations for piston-cylinder apparatus and cubic press were described in previous publications (Liu et al. 2012a; Liu et al. 2012b). The pressure uncertainties, which depend largely on the accuracy of the calibration reaction, were estimated to be less than 5% (Liu et al., 2012a). The experimental temperature was measured and controlled with a $Pt_{94}Rh_6$-$Pt_{70}Rh_{30}$ thermocouple (type B), ignoring the pressure effect on its e.m.f.. Both pressure and temperature were automatically controlled during the experiments. The sample was first pressurized to the target pressure, and then heated at a rate of 100 °C/min. Experiments were quenched by turning off the power, followed by automatic decompression to ambient pressure. From recording temperature with the thermocouple, we found that all experiments were quenched to below 100 °C within 10 seconds. The effect of quenching process on the gaseous phases in the capsule is not discussed here because it is beyond the scope of this study.

The experiments were conducted at higher temperatures (>600 °C) than the conditions of the natural ultra-high-pressure metamorphic rock (<600 °C) to ensure that chemical equilibrium could be achieved over a reasonable duration of the laboratory experiment. Time-series experiments (A-C-2, A-C-3, and A-C-4) were performed at 1.5 GPa and 1000 °C to evaluate phase equilibrium. No significant change in the iron content in the recovered ankerite was observed after a couple of hours, indicating that experiments can reach equilibrium within a couple of hours. Therefore, all other experiments were performed for more than 24 h, which should be sufficiently long to reach equilibrium.

3.4.2. Analyses of experimental products

In order to determine the composition of the gas phases, we collected the gases from the quenched gold capsule using either a piercing device or a crushing device connected to an Agilent 6890A gas chromatograph (GC). The gas chromatograph technique provides definitive identification and quantitative measurement of the hydrocarbons and other gas phases present in the sample with high sensitivity. The gold capsule recovered from the high-pressure experiment was punched with a hard steel needle. The entire capsule was loaded in the valve chamber below the steel needle. We sealed one end of the valve and connected the other end to the GC. The valve chamber was evacuated to high vacuum. We then broke the capsule by rotating the valve handle, and extracted the gases in the capsule to the GC chamber. In most cases, we cannot completely extract gases in the capsule by piercing device because gases may be trapped in the sample. In order to completely extract gases, we loaded the capsule after the piercing method into a small iron tube chamber with one end sealed, and another end connected to the GC. The iron tube chamber was evacuated to high vacuum, and we then crushed the iron tube with a small hand press to extract rest of the gases from the run products to the GC. The details of the analytical method were previously published (Pan et al, 2006). Measurements were performed with an Agilent 6890A gas chromatograph (modified by Wasson ECE Instrumentation) at the State Key Laboratory of Organic Geochemistry, Guangzhou Institute of Geochemistry (Chinese Academy of Sciences). Before each measurement of the extracted gases by the gas chromatograph, we collected the background GC pattern of the instrument to ensure no contamination. The GC analyses were only carried out with the larger recovered samples (~180 mg) from experiments with the 5 mm gold capsule diameters to ensure sufficient amounts of gas phases in the run products for reliable gas content measurements.

After measurement of the gas phases in the capsule using GC, the samples were cut out from the capsule for further analyses. To identify solid phases of the run products, the recovered sample was mounted in epoxy resin and polished for analyses with Raman Spectroscopy, scanning electron microscopy (SEM) and electron probe microanalysis (EPMA). All analyses were performed at the same apparatus and same conditions as described above (Section 3.1) at the MOE Key Laboratory of Orogenic Belt and Crustal Evolution, Peking University.

4. RESULTS

4.1. Petrological observation

4.1.1. Mineral assemblages

The mineral assemblages of carbonated eclogites consist of similar garnet porphyroblasts, fine-grained omphacite matrix, along with varying amounts of minor minerals including carbonate, muscovite, paragonite, glaucophane, epidote, phengite, quartz, and rutile/ilmenite, observed under optical microscope. Poikilitic porphyroblasts of garnets always contain inclusions of omphacite, zoisite, carbonates, and rutile. Subhedral carbonates are dispersed in the matrix or found as inclusions in garnets. The petrographic and geochemical characteristics of carbonated eclogites from S.W. Tianshan subduction zone have been well described in our previous studies (Tao et al., 2014; Tao et al., 2018a).

In this study, we focus on the P-T-fo_2 evolution trend of the S.W. Tianshan subduction zone constrained from the metamorphic mineral assemblages in the carbonated eclogites. In sample K949, different omphacite inclusions were observed in garnet from the core to the rim (Fig. 2a and Table S1). The coexisting garnet and omphacite at different metamorphic stages can be used to constrain a fo_2 evolution trend using garnet and omphacite oxybarometer (Fig. 2d). The P-T evolution trend can also be constrained by a compositional profile of garnet and equilibrated

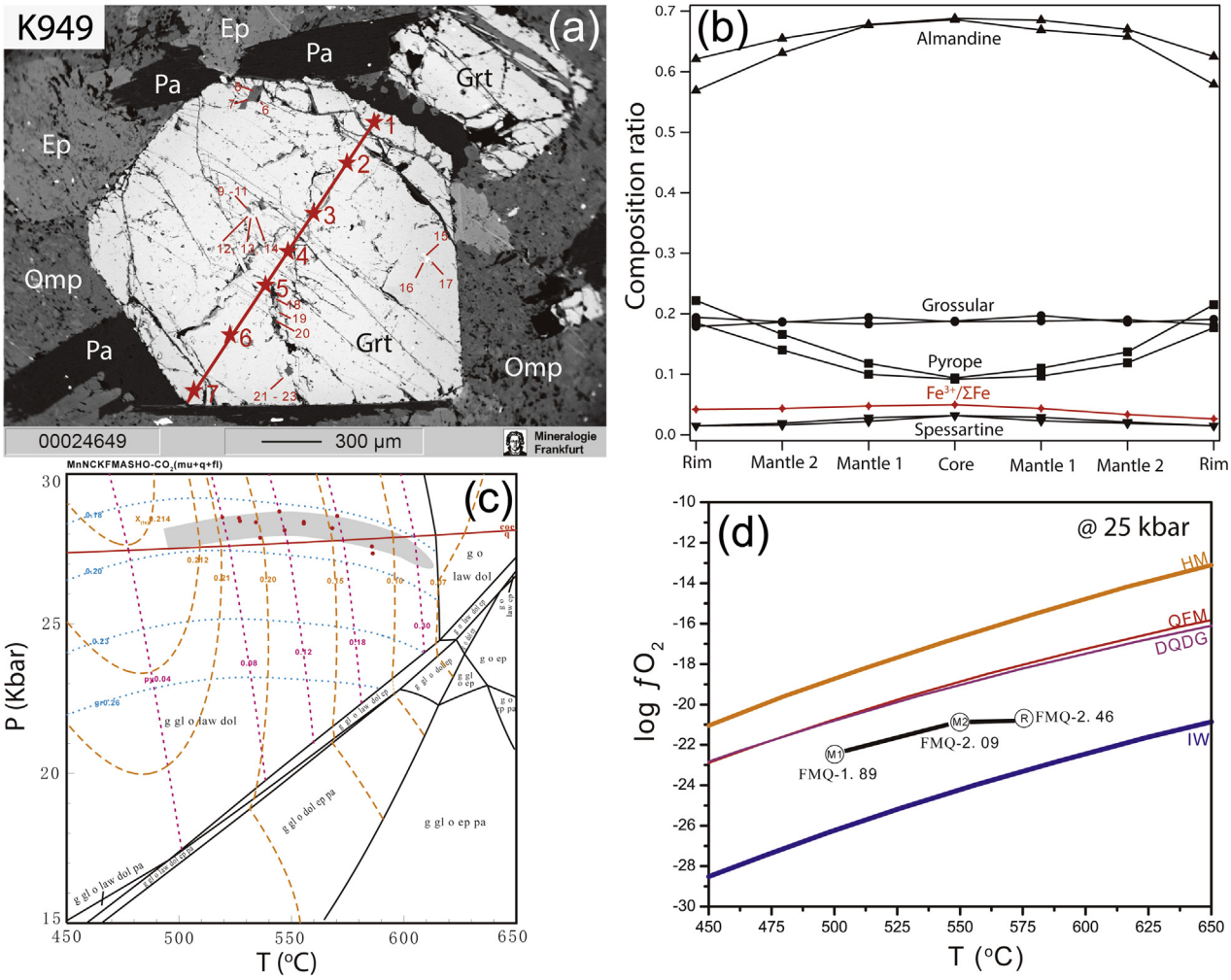

Fig. 2. BSE image, chemical compositions, phase equilibrium modeling, and oxygen fugacity calculation for carbonated eclogite (K949). (a) BSE image of garnet prophyroblast and equilibrated minerals (e.g. omphacite, paragonite, epidotes). Compositional profile of garnet (number 1 to 7 along red line) and its mineral inclusions (number 6 to 23) are marked on the BSE image. (b) Composition profile of garnet prophyroblast: red marks with the line are $Fe^{3+}/\Sigma Fe$ ratio profiles of garnet porphyroblast from "Flank method". (c) P–T pseudosection for K949 calculated in the system NCKMnFMASHO + CO_2. P-T path recorded by garnet compositional profiles is constrained in the P-T phase diagram as a gray belt. (d) Oxygen fugacity evolution trend of carbonated eclogite (K949) constrained by garnet-omphacite oxybarometer in log fO_2 vs. T phase diagram at 25 kbar. The phase boundaries of oxygen fugacity buffers of HM, QFM, DQDG, and IW are thermodynamically calculated using the ThermoCalc program with the improved thermodynamic dataset (Holland and Powell, 2011). (For interpretation of the references to colour in this figure legend, the reader is referred to the web version of this article.)

mineral assemblages (Fig. 2a). In sample H608-23, no omphacite was observed in garnet porphyroblasts in the thin section (Fig. 3c). Although some matrix omphacites were observed in equilibrium with garnet (Fig. 3a), it is hard to assign the f_{O2} from garnet porphyroblast and matrix omphacite to different metamorphic stage. However, in sample H608-23, we observed the reduction reaction from Fe-dolomite to coexisting graphite and magnetite in the matrix (Fig. 3c), which can be used to constrain the fo_2 condition at which the Fe-bearing carbonate was reduced to graphite and magnetite in carbonated eclogite (Fig. 3d). The mineral assemblages of Fe-dolomite, graphite and magnetite were confirmed by typical Raman spectra (Fig. 3b). Remnant of fluid-pockets with deposited graphite was observed in H608-23 (Fig. 3c). The Fe-dolomite in H608-23 shows a slight variation [$Fe^{\#} = Fe/(Fe + Mg) * 100$] ranging from 6 to 10 in Fe concentration (Supplementary Fig. S1). In carbonated eclogite (315-3), garnet porphyroblast and omphacite matrix are predominant minerals with small amounts of rutile and carbonate (Fig. 4a). Some omphacite and minor rutile were also observed in garnet porphyroblast, too.

Supplementary data associated with this article can be found, in the online version, at https://doi.org/10.1016/j.gca.2018.08.008.

4.1.2. Mineral chemistry

Garnets from carbonated eclogite (K949) show compositional and $Fe^{3+}/\Sigma Fe$ ratio zonation from the core to the rim (Table 1 and Fig. 2b), which can be used to reveal

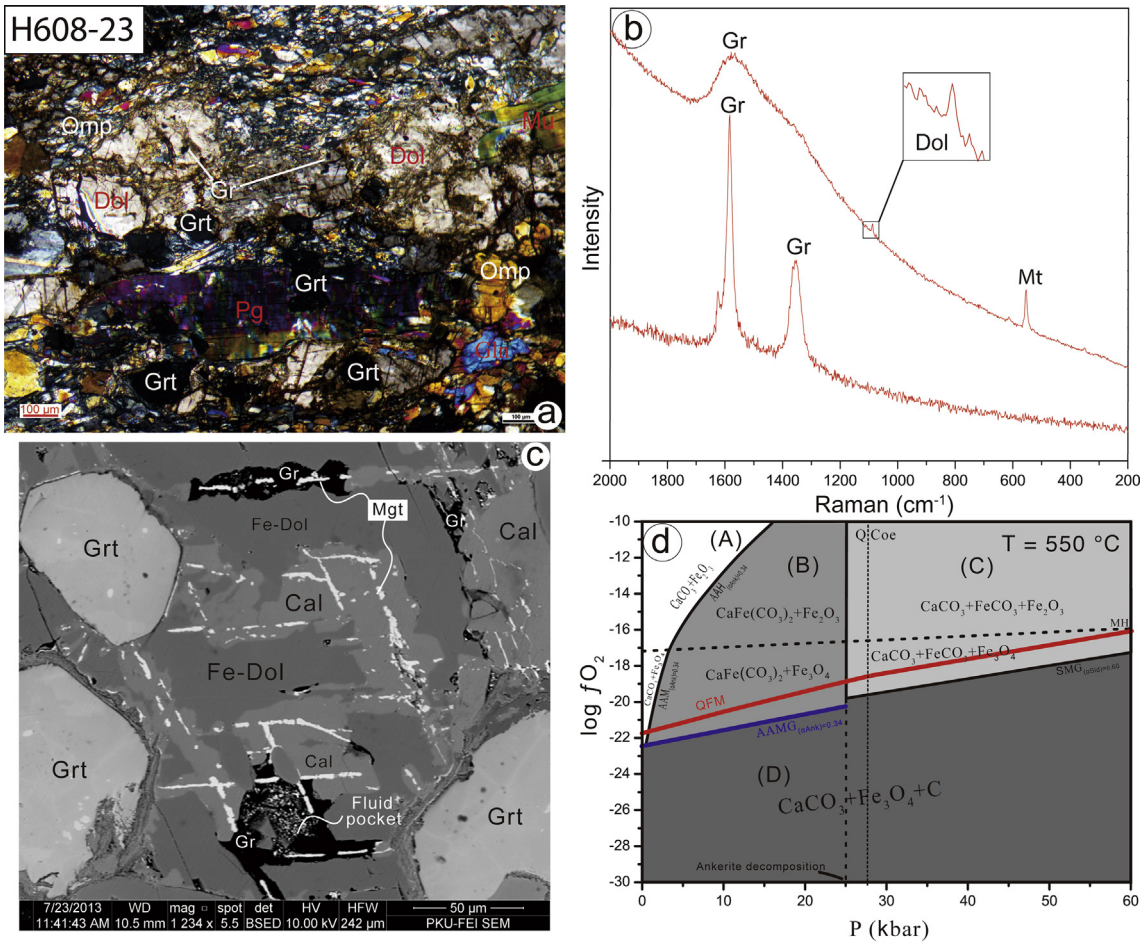

Fig. 3. Photomicrograph, Raman spectrum, BSE image, and oxygen fugacity calculation for carbonated eclogite (H608-23). (a) Photomicrograph of mineral assemblages of H608-23 under crossed polarizing microscopy. (b) Raman spectrum of graphite with dolomite and magnetite in carbonated eclogite (c) BSE image of representative mineral association with graphite associated with fluid-pocket and magnetite (Mgt), surrounded by Fe-dolomite and calcite (Cal), and (d) The calculated P-fO_2 phase diagram in the CaO-FeO-CO_2-O system at 550 °C. In the region A, the ankerite is oxidized into calcite and iron oxide (magnetite or hematite) but without graphite. In the region B, ankerite is coexisting with iron oxide. In the region C, the ankerite will decompose into siderite and aragonite, coexisting with iron oxide. Lowing the oxygen fugacity to the region D, the ankerite reduces to magnetite and graphite. The phase relations were calculated using the ThermoCalc program with the improved internally consistent thermodynamic dataset (Holland and Powell, 2011).

the P, T and fo_2 evolution of carbonated eclogites from S. W. Tianshan subduction zone. These garnets show an increase of pyrope and decrease of almandine from the core to the rim, and a slight decrease of grossular and spessartine from the core to the rim (Table 1 and Fig. 2b). The increase of pyrope coupled with the decrease of grossular and spessartine in garnet from core to rim indicate a typical prograde metamorphism. The $Fe^{3+}/\Sigma Fe$ ratios of garnet profiles in K949 by "Flank method" show a slight decrease from 0.050 to 0.026 from core to rim (Table 1 and Fig. 2b). Na-clinopyroxenes are classified to omphacite in both garnet and matrix according to Morimoto et al. (1988) (Table S1). Amphiboles are glaucophane and barroisite according to the Na-amphibole classification (Leake et al., 1997) (Table S1). The glaucophane porphyroblasts in matrix usually contain inclusions of omphacite, rutile, and carbonate, indicating their formation during the retrograde stage. Phengite/paragonite flakes in the carbonated eclogite are oriented in parallel with the dominant foliation of the specimen. The chemical compositions of typical metamorphic minerals from carbonated eclogites H608-23 and 315-3 are listed in Table S2 for comparison.

4.1.3. Hydrocarbon fluid inclusions

Abundant fluid inclusions were also found in the high-pressure omphacite in sample 315-3 (Fig. 4a), which coexists with garnet. The coexisting garnet also contains tiny fluid inclusions (typically <2 μm). Light hydrocarbons (methane and ethane) were identified in omphacite grains (Fig. 4b). The Raman spectrum of the inclusion bubble in omphacite (Fig. 4c and d) shows characteristic CH stretches at around 2917 cm^{-1}. The observed peak seems to be too broad to be due to the symmetric stretch band of methane alone at 2917 cm^{-1} (cf. Lin et al., 2007). The broad feature is consistent with the additional contribution from the intense doublet of ethane at 2895 cm^{-1} and 2955 cm^{-1}

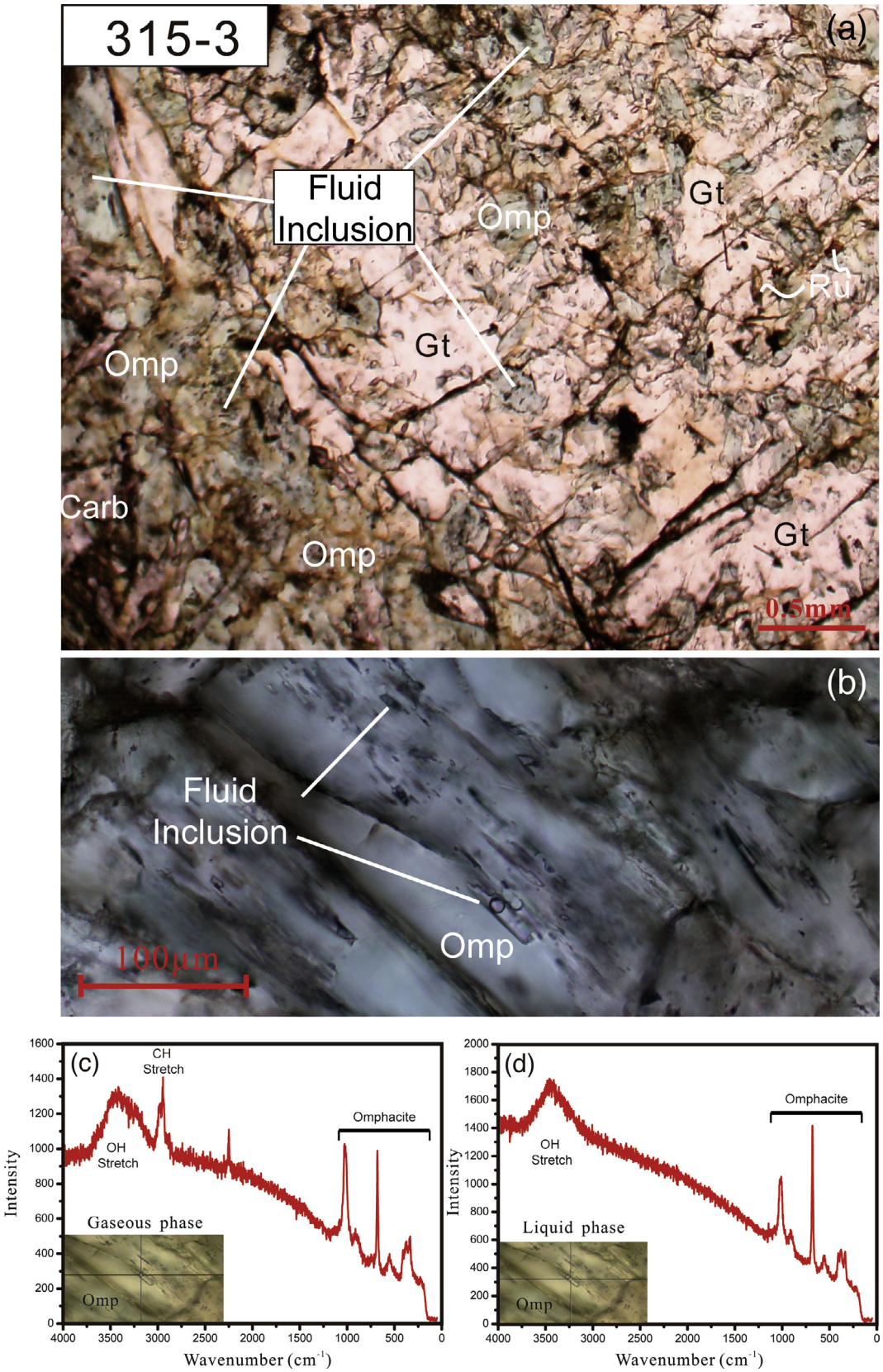

Fig. 4. Microphotograph and Raman spectrum of mineral assemblages and fluid inclusions in carbonated eclogite (315-3). (a) Photomicrograph of mineral assemblages in the carbonated eclogites (315-3) under polarizing microscopy. (b) Optical microphotograph of a thin section showing methane/ethane-bearing fluid inclusions in omphacite (Omp) from carbonated eclogite (315-3). (c) Raman spectrum of the gas phase showing the CH stretches from methane and ethane. (d) Raman spectrum of the fluid phase showing OH stretch only.

Table 1
Chemical compositions of garnets in carbonated eclogite (K949).

	Sample	Gt1_1	Gt1_2	Gt1_3	Gt1_4	Gt1_5	Gt1_6	Gt1_7	Gt2_1	Gt2_2	Gt2_3	Gt2_4	Gt2_5	Gt2_6	Gt2_7
Composition	SiO_2	38.27	37.86	37.63	37.52	37.73	37.80	38.35	38.48	38.23	37.74	37.72	37.83	38.01	38.57
	TiO_2	0.04	0.06	0.10	0.06	0.08	0.07	0.04	0.02	0.04	0.06	0.08	0.08	0.06	0.03
	Al_2O_3	22.06	21.76	21.59	21.56	21.63	21.71	22.14	22.24	22.03	21.70	21.58	21.69	21.78	22.13
	Cr_2O_3	0.01	0.01	0.01	0.01	0.01	0.02	0.01	0.02	0.01	0.01	0.06	0.01	0.02	0.01
	FeO	28.08	29.40	30.18	30.54	30.48	29.96	28.29	26.00	28.62	30.38	30.67	29.98	29.61	26.49
	MnO	0.67	0.83	1.24	1.42	1.28	0.93	0.69	0.69	0.72	0.97	1.43	1.03	0.83	0.68
	NiO	0.00	0.00	0.00	0.00	0.00	0.00	0.00	0.00	0.00	0.00	0.00	0.00	0.00	0.00
	MgO	4.69	3.53	2.50	2.30	2.43	2.97	4.50	5.69	4.23	2.97	2.35	2.77	3.46	5.53
	CaO	6.30	6.53	6.73	6.47	6.53	6.62	6.45	6.92	6.62	6.41	6.57	6.89	6.55	6.82
	Na_2O	0.04	0.04	0.07	0.04	0.04	0.04	0.04	0.04	0.04	0.04	0.03	0.04	0.04	0.04
	Total	100.17	100.02	100.06	99.92	100.21	100.13	100.51	100.10	100.54	100.28	100.48	100.31	100.36	100.31
cpfu	Si	2.99	2.99	2.99	2.99	3.00	2.99	2.99	2.99	2.99	2.99	2.99	2.99	2.99	2.99
	Ti	0.00	0.00	0.01	0.00	0.00	0.00	0.00	0.00	0.00	0.00	0.00	0.00	0.00	0.00
	Al	2.03	2.03	2.02	2.03	2.03	2.03	2.04	2.03	2.03	2.03	2.02	2.02	2.02	2.02
	Cr	0.00	0.00	0.00	0.00	0.00	0.00	0.00	0.00	0.00	0.00	0.00	0.00	0.00	0.00
	Fe	1.84	1.94	2.01	2.04	2.02	1.98	1.85	1.69	1.87	2.01	2.04	1.98	1.95	1.72
	Mn	0.04	0.06	0.08	0.10	0.09	0.06	0.05	0.05	0.05	0.06	0.10	0.07	0.06	0.04
	Ni	0.00	0.00	0.00	0.00	0.00	0.00	0.00	0.00	0.00	0.00	0.00	0.00	0.00	0.00
	Mg	0.55	0.42	0.30	0.27	0.29	0.35	0.52	0.66	0.49	0.35	0.28	0.33	0.41	0.64
	Ca	0.53	0.55	0.57	0.55	0.56	0.56	0.54	0.58	0.55	0.54	0.56	0.58	0.55	0.57
	Na	0.01	0.01	0.01	0.01	0.01	0.01	0.01	0.01	0.01	0.01	0.00	0.01	0.01	0.01
	Total	7.99	8.00	7.99	7.99	7.99	7.99	7.99	8.00	8.00	8.00	7.99	7.99	7.99	8.00
Flank Method	$Fe^{3+}/\Sigma Fe$	0.026	0.030	0.037	0.034	0.038	0.032	0.033	0.042	0.043	0.048	0.050	0.044	0.033	0.026
	FeO	27.35	28.53	29.07	29.51	29.33	29.00	27.35	24.91	27.38	28.93	29.14	28.67	28.62	25.79
	Fe_2O_3	0.82	0.97	1.23	1.15	1.28	1.06	1.05	1.21	1.38	1.60	1.70	1.45	1.10	0.78

Note: Chemical compositions from electron probe are in wt%. The cations per formula unit (cpfu) are normalized to 12O.

(*e.g.*, Atamas et al., 2004), shown as the shoulders on both sides of the 2917 cm^{-1} methane peak, marked with a tick in Fig. 4c and d. The broad peak at 3440 cm^{-1} is due to the OH stretch. Only the OH stretch was detected in the fluid phase (Fig. 4c and d), indicating H_2O-dominated fluid inclusion with low gas solubility. All peaks at wavenumbers below 1200 cm^{-1} can be indexed based on the Raman spectrum of omphacite with the most intense peak at 681 cm^{-1} (Fig. 4c and d).

The fluid inclusions in omphacite with non-planar populations are tubular with their long dimension parallel to the c-axis of the omphacite crystals (Fig. 4b). These features suggest that they are primary inclusions trapped during the growth of omphacite at the high-pressure metamorphic event (Gao and Klemd, 2001). They are also characterized by low salinity (~ 4 wt% NaCl equivalent), estimated from freezing-point depression using the Linkam THMS600 heating and freezing stage. The likely carbon source of the fluid inclusions is from predominant carbon-bearing phases (carbonate) in carbonated eclogite. Similar fluid inclusions (no hydrocarbon) associated with daughter carbonate were reported in eclogite from S.W Tianshan subduction zone (see Fig. 4 in Gao et al. (2007)).

4.1.4. *P - T - fo_2 evolution*

The calculated pseudosection for carbonated eclogites (K949) using bulk-rock composition is contoured with isopleths of grossular and pyrope contents in garnet (Fig. 2c). In the possible mineral assemblage region, the grossular content decreases obviously with an increase of pressure, while the pyrope content increases with an increase of temperature. The chemical composition profiles of two garnet grains in K949 were plotted on the thermodynamic pseudosection to constrain the metamorphic P-T path of this carbonated eclogite (gray belt in Fig. 2c). Garnet compositions were plotted in the dolomite- and glaucophane- bearing lawsonite eclogite region, which is consistent with the mineral assemblages observed by optical microscopy (Fig. 2a). The slight decrease of grossular profile indicates almost isobaric process (at ~25 kbar), while the obvious increase of pyrope content indicates a heating process from ~500 to ~575 °C (Fig. 2c). In other words, the garnet profiles in K949 record an isobaric heating prograde process (gray belt in Fig. 2c).

Omphacite inclusions at different metamorphic stages were observed in garnets from mantle to rim in K949 (Fig. 2a and Table 1). Along the garnet growing zonation, we chose three garnet-omphacite pairs to constrain the oxygen fugacity evolution trend using equilibrium: $5CaFeSi_2O_6$ (clinopyroxene) + $1/3Ca_3Al_2Si_3O_{12}$ (garnet) + O_2 = $2Ca_3Fe_2Si_3O_{12}$ (garnet) + $1/3Fe_3Al_2Si_3O_{12}$ (garnet) + $4SiO_2$ (coesite) (Stagno et al., 2015). The calculated P-T conditions were used to calculate the oxygen fugacities. We calculated the oxygen fugacities at 500, 550, 575 °C and ~25 kbar using the garnet-omphacite oxybarometer for K949 (Fig. 2d). The constrained oxygen fugacities were corrected for the presence of quartz, rather than coesite which implies a correction of ~−0.3 log units. These fo_2 showed a decrease from FMQ-1.89 to FMQ-2.46 via FMQ-2.09 falling into the graphite stability field

(Fig. 2d). Garnet and its omphacite inclusions in K949 recorded a decreased oxygen fugacity during the prograde isobaric heating process.

We observed the reduction structure of Fe-bearing dolomite into aragonite, magnetite, and graphite in the carbonated eclogite (H608-23) (Fig. 3c), which was used to constrain the fO_2. Fig. 3d shows the estimated oxygen fugacity from the reduction reaction of Fe-bearing dolomite into aragonite, magnetite, and graphite. The upper bound of the oxygen fugacity for the carbonated eclogite H608-23 is constrained by the reaction of ankerite = calcite + magnetite + graphite + O_2 ($ACMG_{H608\text{-}23}$, blue[1] line in Fig. 3d). The activity of ankerite ($\alpha_{Ank} = 0.34$) is determined on the basis of microprobe analyses of the composition of Fe-bearing dolomite according to the solid solution model of dolomite and ankerite (White et al., 2003). The calculated value (blue line) is lower than QFM buffer (red line) by about 1.5 log units (Fig. 3d). The fO_2 (<~FMQ-1.5) constrained for reduction of carbonate to graphite in the carbonated eclogite in this study is very consistent with experimental work (see Fig. 8 in Stagno et al. (2015)).

4.2. High-pressure experimental results

Table 2 lists the experimental conditions and the observed phases in the recovered samples. We have observed a number of hydrocarbons including methane, ethane, and propane in all of the recovered samples (Table 3). Fig. 5 shows a representative gas chromatogram with a flame ionization detector, indicating the presence of CH_4, C_2H_6, and C_3H_8 in the recovered sample (A-C-7). Table 3 shows the measured gas contents for all of the large samples (5-mm capsule). The efficiency of extracting gas phases from run products depends on the interconnectivity of the pores and fracture distribution in the quenched samples. The needle-piercing method yielded extremely high values for CO_2 gas. The total amounts of gases extracted from the piston-cylinder experiment is relatively high, especially in which siderite was also obs*f*erved, but very low values for the total amounts of gases extracted from the multi-anvil experiments (Table 3). The difference could indicate significant differences in pore distribution and fractures between the recovered piston-cylinder and multi-anvil samples. For the multi-anvil samples, the needle-piercing method alone produced very low yields of the gas phases (<0.005 mL). Therefore, the measured values and ratios are less reliable. A combination of piercing and crushing of the entire sample significantly increased the efficiency of gas extraction, yielding about 10 times more gases released from the samples (~0.05 mL) and producing more consistent results on the gas extraction. The emphasis of the analyses is on positive identification of the gas phases in the run products for this study. It is difficult to assess the full production of the gas phases because of possible incompleteness of gas extraction and unknown initial water content. However, the ratios of different gases may provide some insights into the general trends of gas production as functions of oxygen fugacity, pressure, and temperature. CO_2 is the dominant gas in all the recovered samples, accounting for more than 96 % of the total measured gases. Among the detected hydrocarbons, methane is always the dominant hydrocarbon component although considerable amounts of ethane and propane were also detected in the run A-C-6 recovered from 4 GPa and 1200 °C (Table 3). Coincidently, this run also showed the lowest $Fe^{\#}$ in the recovered ankerite among the large-capsule experiments (Table 2).

All experiments at pressures from 1 to 6 GPa at 600–1200 °C produced the solid phase assemblage including ankerite (Ank), graphite (Gr), and magnetite (Mgt) (Table 2). The recovered samples from low pressure (<2 GPa) experiments contain many relatively large voids (up to 50 μm), partially filled with graphite (Fig. 6). The voids must have been filled with fluid/gas phases together with graphite during the experiments. Fluid inclusions in ankerite were easily identified by the optical microphotograph (Fig. 6c), and Raman spectra of the fluid inclusions were collected. Fig. 6d shows a representative Raman spectrum of the fluid inclusion, which shows the characteristic CH stretches at around 2917 cm^{-1} together with the peaks of graphite and ankerite. The Raman spectrum in the CH stretch region is very similar to that of the natural fluid inclusion. We interpret the broad feature of the Raman peak as the result of contributions from the methane symmetric stretch band at 2917 cm^{-1} together with the doublet of ethane at 2895 cm^{-1} and 2955 cm^{-1}. The presence of methane and ethane in the synthetic fluid inclusion is further supported by independent measurements using gas chromatography. Presence of graphite in the run products was confirmed on the Raman spectra and EDS elemental mapping (Fig. 6a and d), indicating a graphite-saturated fluid. The solid phase assemblage of ankerite, magnetite, and graphite is also confirmed by X-ray diffraction measurements and with SEM (scanning electron microscope) analyses (Fig. 5b). The Fe content in the recovered ankerite is lower than that of the starting material, indicating loss of iron to form magnetite (Table 2). The Fe contents of the starting material Fe-dolomite generally decrease with both time (Fig. S2a) and temperature (Fig. S2b), which is comparable with that from naturally carbonated eclogite (H608-23; Fig. S1).

4.3. Formation reaction for abiotic hydrocarbons

McCollom (2003) experimentally studied the siderite ($FeCO_3$) decomposition in the presence of water vapor at 300 °C and ambient pressure, and generated a variety of organic products dominated by alkylated and hydroxylated aromatic compounds. The overall reaction for synthesis of the hydrocarbons from siderite is suggested as:

$$3FeCO_3 + wH_2O \Rightarrow Fe_3O_4 + xCO_2 + yCO + zH_2 + \text{organic compounds} \quad (1)$$

where w, x, y, and z are undetermined stoichiometric coefficients.

A similar reaction was suggested by Milesi et al. (2015) as

[1] For interpretation of color in Fig. 3, the reader is referred to the web version of this article.

Table 2
Experimental conditions and run products.

Run#	Capsule dia. (mm)	P (GPa)	T (°C)	Time (hr)	Run products	$Fe^{\#}$ of Ank
A-C-0	2.5	1	600	120	Ank, Gr, Mgt, fluid	15
A-C-5	2.5	1.5	900	48	Ank, Gr, Mgt, fluid	16
A-C-2	2.5	1.5	1000	3	Ank, Gr, Mgt, fluid	10
A-C-3	2.5	1.5	1000	8	Ank, Gr, Mgt, fluid	9
A-C-4	2.5	1.5	1000	36	Ank, Gr, Mgt, fluid	8
A-C-1	2.5	2	850	25	Ank, Gr, Mgt, fluid	25
A-C-7	5	1.5	800	72	Ank, Gr, Mgt, Sd, fluid	24
A-C-6	5	4	1200	24	Ank, Gr, Mgt, fluid	23
A-C-8	5	4	1000	24	Ank, Gr, Mgt, fluid	24
A-C-9	5	6	1000	24	Ank, Gr, Mgt, fluid	24
A-C-10	5	6	1200	24	Ank, Gr, Mgt, fluid	24

Two gold capsule diameters were used, OD = 5 mm and OD = 2.5 mm. Mineral abbreviations: Ank, ankerite; Gr, graphite; Mgt, magnetite; and Sd, siderite. Fluid compositions are shown in Table 3. The value of $Fe^{\#}$ is defined by $Fe^{\#} = [Fe^{2+}/(Ca + Mg + Fe^{2+} + Mn)] \times 100$ and the $Fe^{\#}$ of the starting material ankerite is 26.

Table 3
The measured gas contents by gas chromatograph (mL).

P(GPa)-T (°C) Gas species	1.5–800 A-C-7[§]	6–1000 A-C-9[§]	4–1000 A-C-8[†]	4–1200 A-C-6[†]	6–1200 A-C-10[†]
CH_4	0.000692	0.002167	0.000632	0.000417	0.000417
C_2H_6	0.00025	0.000107	0.000039	0.000241	0.000015
C_2H_4	–	–	0.000045	0.000241	0.000028
C_3H_8	0.000146	0.000013	–	0.000153	–
C_3H_6	–	–	0.000024	0.000153	0.000018
I-C_4H_{10}	–	–	–	0.000112	–
N-C_4H_{10}	–	–	–	0.000112	–
C_4H_8	–	–	0.000014	0.000112	–
H_2	0.005254	0.001198	–	0.000109	0.000443
Total reduced gas	0.006342	0.003485	0.000754	0.00165	0.000921
CO_2	0.206385	0.00092	0.054095	0.046266	0.046241
Total	0.212727	0.004405	0.054849	0.047916	0.047162
Total reduced gas /Total	0.03	0.79	0.01	0.03	0.02

[§] Gas extracted by the needle piecing method.
[†] Gas extracted by combining the needle piecing and sample crashing method; I-C_4H_{10}, isohexane; N-C_4H_{10}, normal hexane. The uncertainty for the measured gas content is about 0.5% (Pan et al., 2006).

$$3FeCO_3 + H_2O = Fe_3O_4 + 3CO_2 + H_2 \quad (2)$$

from an experimental study of the system siderite and water at 200 and 300 °C under a pressure of 50 MPa. In our study, the predominant carbonate observed in natural eclogites from S.W. Tianshan subduction zone is Fe-bearing dolomite (ankerite): $Ca(Mg_{1-a}, Fe_a)(CO_3)_2$, where a is Fe/(Fe + Mg) in the dolomite. Similar Fe-bearing dolomite was used as the starting material for the high-pressure simulations in this study. The oxidized iron (Fe_3O_4) and reduced carbon species (e.g. graphite and hydrocarbons) were documented in both field specimen and the recovered experimental charges. Also, a variety of Fe concentrations in Fe-bearing dolomite was observed in both natural and experimental samples in our study. Based on previous low-T and low-P experiments (McCollom, 2003; Milesi et al., 2015), and petrological observation and high-P experimental simulation in our study, the possible chemical reaction for the formation of hydrocarbons can be written as:

$$\begin{aligned} &Ca(Mg_{1-a}, Fe_a)(CO_3)_2 + wH_2O \\ &\Rightarrow Ca(Mg_{1-b}, Fe_b)(CO_3)_2 + (a-b)/3Fe_3O_4 + xCO_2 \\ &\quad + yC + zH_2 + gC_nH_{2n+2} + fCa^{2+} \\ &\quad \text{-bearing COH fluid} \end{aligned} \quad (3)$$

where a and b are Fe/(Fe + Mg) of starting and product Fe-bearing dolomite, a is greater than b in this study, and w, x, y, z, g, and f are undetermined stoichiometric coefficients.

The starting material for our experiments is natural Fe-dolomite (Ankerite). Its chemical formula is $Ca_{1.02}(Fe_{0.52}Mg_{0.43}Mn_{0.04})(CO_3)_2$. The initial $Fe^{\#} = [Fe^{2+}/(Ca + Mg + Fe^{2+} + Mn)] \times 100$ of the starting material is 26 (Table 2). After the experiments, the $Fe^{\#}$ of ankerite in the run products decreased to a value as low as 8. This indicates that the $FeCO_3$ component in $Ca_{1.02}(Fe_{0.52}Mg_{0.43}Mn_{0.04})(CO_3)_2$ is the fundamental reactant for the redox reaction. The mechanism of the redox reaction is similar to McCollom (2003)

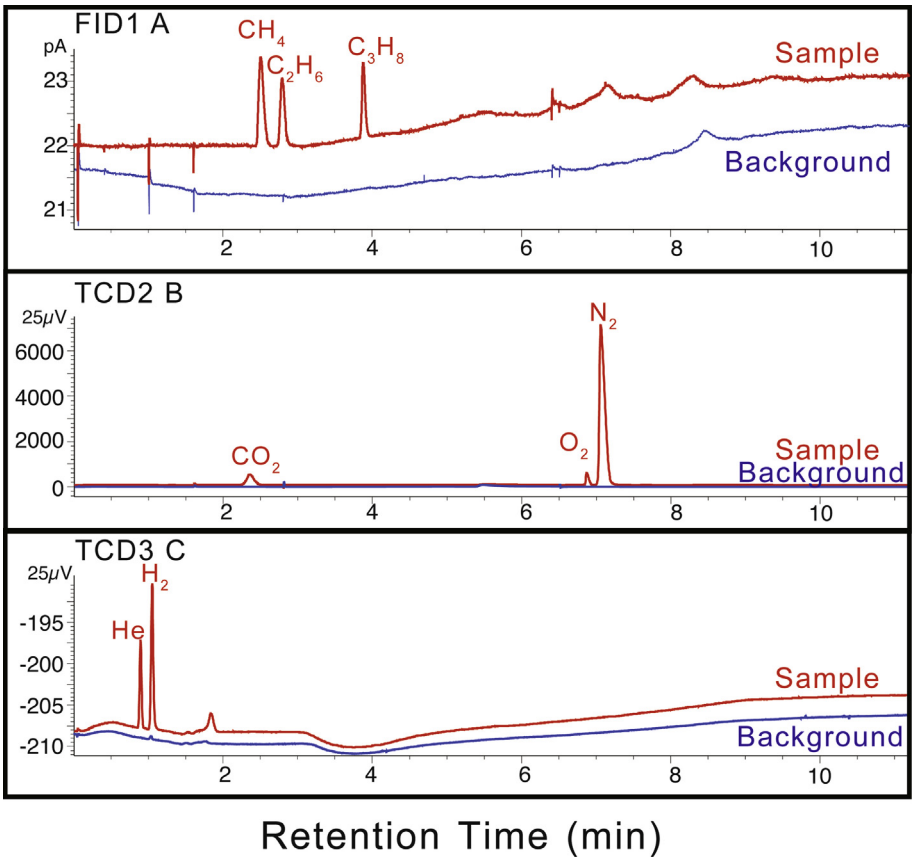

Fig. 5. EDS elemental mapping, BSE images, optical microphotograph, Raman spectrum of run products from high-pressure experiments. (a and b) EDS elemental (carbon) mapping and BSE image indicating formation of abundant of graphite and magnetite in experiment A-C-7. (c) Optical microphotograph of the run A-C-4 showing assemblage of ankerite (Ank), magnetite (Mgt) and graphite (Gr). Small fluid inclusions in ankerite are visible and large voids filled with graphite are distributed throughout the sample. (d) Raman spectrum of a fluid inclusion in the run A-C-4 showing CH stretches of methane and ethane along with Raman peaks of graphite and ankerite.

and Milesi et al. (2015) except that the activity of the $FeCO_3$ component in $Ca_{1.02}(Fe_{0.52}Mg_{0.43}Mn_{0.04})(CO_3)_2$ is depending on the activity model and chemical composition of the ankerite. The dissolved Ca and Mg cations in the fluid may also have some effect on the synthesis of abiotic hydrocarbons at high PT conditions (McDermott et al., 2016).

5. DISCUSSION

5.1. Decreased fO_2 of the subduction zone and its effect on the deep carbon cycle

The fO_2 of the asthenospheric mantle below mid-ocean ridges was constrained by the oxy-barometer of abyssal peridotites (Bryndzia and Wood, 1990) and $Fe^{3+}/\Sigma Fe$ ratios of MORB basaltic glass (Bézos and Humler, 2005) to be close to FMQ-1 (Christie et al., 1986; Frost and McCammon, 2008). However, the fO_2 of the mantle wedge above subducting slabs, whose fO_2 is always from FMQ to FMQ + 2, including substantial proportion with $fO_2 >$ FMQ + 1, is often summarized as being more oxidized than asthenospheric mantle (Frost and McCammon, 2008 and references therein). These more oxidized values are usually attributed to the addition of more oxidizing matters (e.g. H_2O) from subduction zones (Parkinson and Arculus, 1999; Wood and Virgo, 1989; Bézos and Humler, 2005; Malaspina et al., 2009; Kelley and Cottrell, 2009). Therefore, a relatively oxidized condition for subduction zones is generally proposed. However, until now, only few studies constrained the real in situ fO_2 of a subduction zone because the oxygen fugacity of the subduction zone is complex (Foley, 2011). Metamorphic rocks in the subduction zone always have a wider range of possible fO_2 values than most igneous rocks. Meanwhile, at different metamorphic stages in the subduction zone, the oxygen fugacity varies a lot (Donohue and Essene, 2000).

The oxidation state of initial oceanic MORB slabs (FMQ-1) is affected by hydrothermal alteration (e.g. hydration) and sedimentation before entering the subduction zone. Normally, the oxidation state of altered oceanic crust before subduction is estimated between FMQ-1 and FMQ (Foley, 2011). Subduction of altered oceanic crust, which is metamorphosed to (carbonated) eclogites at pressure >1 GPa, is the major mechanism by which carbon enters the mantle. The fO_2 evolutions of subducting slabs should have a significant effect on the stability and speciation of carbon-bearing phases in subduction environments

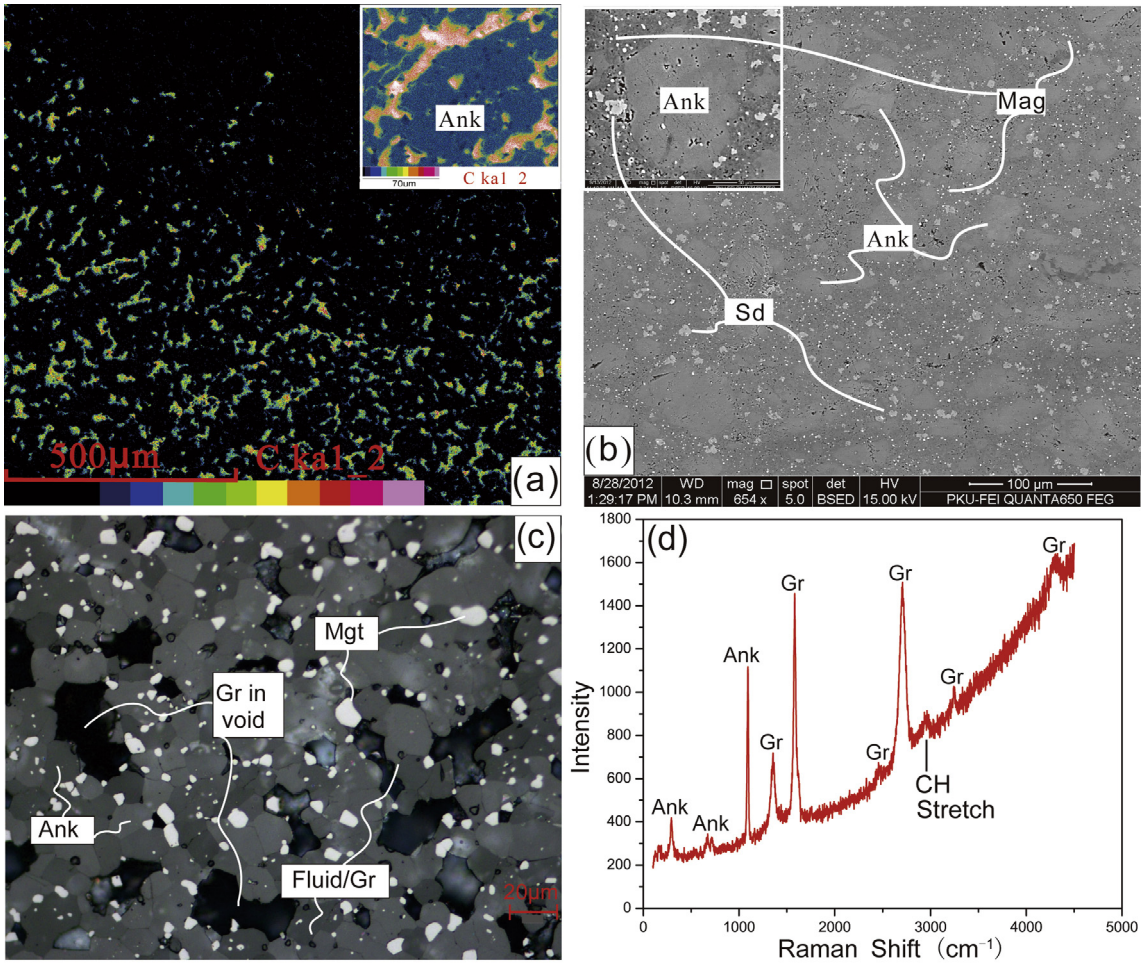

Fig. 6. Representative gas chromatograms of the extracted gases from the quenched sample (A-C-7) with background measurements. The gas hydrocarbons including CH_4, C_2H_6, and C_3H_8 were analyzed with the flame ionization detector (FID) and the other gases were analyzed with two thermal conductivity detectors (TCD). Helium (He) and nitrogen (N2) were used as the carrier gases. The modified gas chromatograph (GC) is equipped with a flame ionization detector (FID) for hydrocarbon analysis and two thermal conductivity detectors (TCD) for analyzing hydrogen, CO_2, and other inorganic gases.

(Aulbach and Stagno, 2016). In this study, we constrained the fO_2 evolution trend of S.W. Tianshan subduction zones by different oxy-barometers in situ. Fig. 7 shows the fO_2 of the S.W. Tianshan subduction zone, compared with those in other geological environments. A slightly decreased fO_2 (from FMQ - 1.9 to FMQ - 2.5) was recorded for prograde metamorphism of the S.W. Tianshan subduction zone using the garnet-omphacite oxy-barometer. This low fO_2 range is also consistent with the low oxygen fugacity (<~FMQ - 1.5) constrained by the observed reduction reaction from Fe-bearing dolomite to calcite, magnetite, and graphite. In comparison with the oxygen fugacity of DQDG (dolomite + 2 quartz = diopside + 2 graphite + $2O_2$) in Fig. 7, which controls the formation of graphite from the reduction of carbonate in carbonated eclogite assemblages (Luth 1993; Stagno et al., 2015), the oxygen fugacity of S.W. Tianshan is relatively low. This is consistent with ubiquitous graphite in meta-ophiolites from S. W. Tianshan subduction zone (Lü et al., 2013). Further, the C-H_2O oxygen fugacity buffer, separating CH_4- and CO_2-rich aqueous fluid ($X_O = 1/3$), was also shown (C-H_2O in Fig. 7), calculated using the COH model (Zhang and Duan, 2009). Below this boundary, abiotic hydrocarbon will form from C-H-O fluid. This is another constraint for the formation of abiotic hydrocarbon in the S.W. Tianshan subduction zone. The observed oxygen fugacity of the S.W. Tianshan subduction zone is also comparable to that of the Alpine Corsica where the abiotic production of reduced graphite in subduction zones during decarbonation was suggested (Galvez et al., 2013; Malvoisin et al., 2011). An increased retrograde fO_2 (FMQ + 1) was constrained by rutile-ilmenite oxy-barometers for eclogites from the S. W. Tianshan subduction zone (Tao et al., 2017b). In comparison to redox conditions of other subduction belts, the S.W. Tianshan subduction zone has the lowest oxidation condition. If the initial fO_2 of the S.W. Tianshan subduction zone is comparable to a normal altered oceanic crust (between FMQ-1 and FMQ; Foley, 2011), there would be a continuous decrease of fO_2 for the S.W. Tianshan subduction zone during the subduction process to evolve

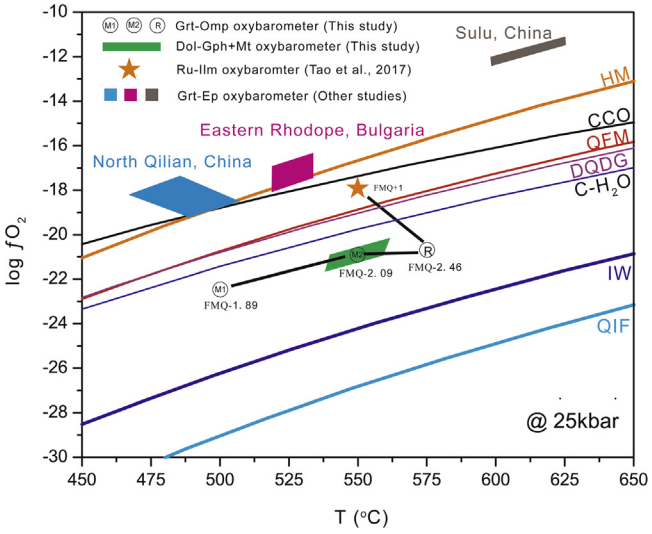

Fig. 7. Comparisons of the estimated oxygen fugacity for different subduction zones. The oxygen fugacity evolution trend of S.W Tianshan subduction zone was constrained by the garnet-omphacite oxybarometer (from M1 to M2, then to R), Fe-dolomite-graphite and magnetite oxybarometer (blue marker), and rutile-ilmenite oxybarometer (orange star). The estimated values of oxygen fugacity for other subduction zones (Eastern Rhodope, Bulgaria; Sulu, China; and North Qilian) were shown for comparison. They have much higher oxygen fugacity than the Southwestern Tianshan subduction zone. The oxygen fugacity of North Qilian is constrained by the garnet-epidote oxybarometer (Mattinson et al., 2004; Cao et al., 2011), whereas the oxygen fugacity of Sulu, China and Eastern Rhodope, Bulgaria are constrained by the garnet peridotite oxybarometer (Malaspina et al., 2009). The C-H_2O oxygen fugacity buffer at 550 °C, separating CH_4- and CO_2-rich aqueous fluid ($X_O = 1/3$), was also shown, calculated using the COH model of (Zhang and Duan, 2009). Other oxygen fugacity buffers (CCO, DQDG, HM, IW, QIF and QFM) were calculated using the ThermoCalc program with the improved internally consistent thermodynamic dataset (Holland and Powell, 2011).

to relatively reduced condition, ranging from FMQ-1.9 to FMQ-2.5. The continuous decrease of fO_2 the subduction zone may result from releasement of oxidized fluid from subducting slabs to the overlying mantle wedge. This is also suggested by previous petrological record by meta-ophiolite from Alps metamorphic belts (Borfecchia et al., 2012; Debret et al., 2014). In other hands, carbonated eclogites have been shown to become more and more reduced as the effect of pressure on the incorporation of Fe^{3+} in garnet (Stagno et al. 2015).

The change of redox state of the carbonated slabs during the subduction process should have a big effect on the deep carbon cycle in the subduction zone. The decreased fO_2 of the subduction zone can explain the formation of reduced carbon-bearing phases (e.g. graphite and methane/ethane) from carbonate reduction in the subduction zone (e.g. S. W. Tianshan subduction zone). The decrease of fO_2 by a possible dehydration-redox reaction during the subduction process (Borfecchia et al., 2012; Debret et al., 2014) will transfer carbonate into graphite. The redox reaction can also change the mobility of carbon-bearing phases from mobile carbonate to immobile graphite in the subduction. This will strongly affect the carbon cycle behavior in the subduction zone. On the other hand, several studies showed the origin of diamonds from deep mantle to be closely linked with the recycled carbonated oceanic crust (Thomson et al., 2014; Kiseeva et al., 2016; Xu et al., 2017; Kiseeva et al., 2018). The generally higher abundances of diamonds are associated with eclogites and with the high proportion of inclusions of eclogitic association in some diamond populations (Cartigny, 2005). Numerous geochemical and isotope studies showed that the deep diamond and its inclusions inherited the characteristic of recycled carbonated slabs (Ickert et al., 2013; Kiseeva et al., 2016). The recycled carbonate would be an important carbon source for deep mantle diamond, too.

5.2. Abiotic hydrocarbons in the subduction zone

Carbonates are the predominant carbon-bearing phases that are commonly present in the subducted slab. They are the potential source of carbon for the abiotic formation of light hydrocarbons and graphite in the subduction zone. We have limited knowledge about the abiotic synthesis of hydrocarbons from carbonates at high pressure and temperature relevant to subduction zones. McCollom (2003) described thermal decomposition of siderite in the presence of water vapor at 300 °C and demonstrated abiotic synthesis of organic compounds dominated by alkylated and hydroxylated aromatic compounds. Milesi et al. (2015) investigated the chemical processes governing the carbon speciation associated to hydrothermal decomposition of siderite at 200–300 °C and a pressure of 50 MPa, and showed that the gas phase was dominated by CO_2, H_2, and CH_4. These results are complementary to our findings at higher temperatures and pressures. Our results indicate that the formation of hydrocarbons in the system over wide P-T conditions, although the quantification and kinetics of the reactions require further investigation.

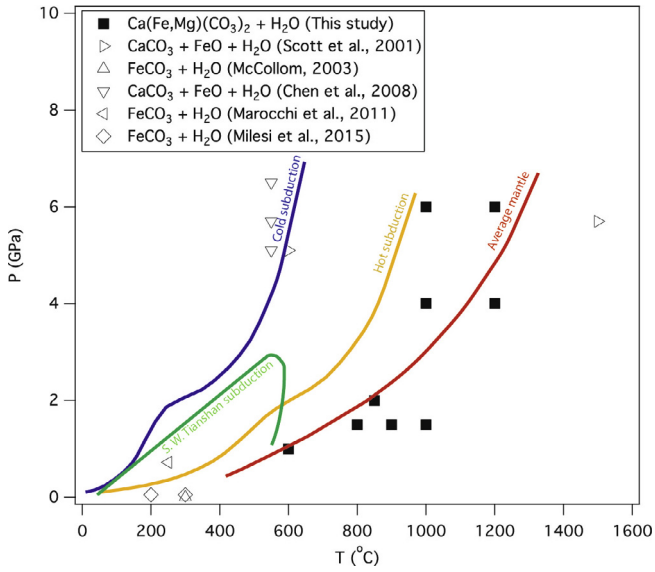

Fig. 8. Summary of P-T conditions of experimental runs in this study in comparison with those from previous studies in similar systems (Scott et al., 2004; McCollom, 2003; Chen et al., 2008; Marocchi et al., 2011; Milesi et al., 2015). Typical subduction and mantle geotherm from Tao et al. (2013), and S.W. Tianshan subduction path is also plotted for comparison.

Previous high-pressure experiments on methane formation from the carbonate-H_2O reaction were also performed in a tiny diamond-anvil cell chamber ($<7 \times 10^{-4}$ mm^3) at pressures above 5 GPa (Scott et al., 2004; Chen et al., 2008). The experiments at temperatures below 600 °C (Chen et al., 2008) were conducted in the resistance-heated diamond-anvil cells, whereas the experiments at higher temperature and pressure were performed using the laser-heating technique (Scott et al., 2004) that have issues such as stable temperature control. Raman spectroscopy was the only diagnostic technique used for the identification of the hydrocarbon compounds. In the experiments of Chen et al. (2008), the reduction of calcite ($CaCO_3$) to form methane was achieved by adding the reducing agents including FeO, SiO, and natural fayalite to water. The characteristic CH stretches were observed by in-situ Raman measurements. Diamond-anvil cell experiments provide excellent in-situ measurements, but they are not ideal for hydrocarbon synthesis because of potential contamination from the diamond anvils (Chou and Anderson, 2009) and the small sample volume. In this study, we used Fe-bearing dolomite (ankerite) and H_2O for the experiments, sealed in a large gold capsule (~150 mm^3), at least 200 thousand times larger than the diamond-anvil cell chamber, allowing conventional gas content measurements. The reduced carbon species including graphite and hydrocarbons are formed by a disproportionation reaction of Fe^{2+}-bearing ankerite and H_2O, accompanied by the formation of Fe^{3+}-bearing oxide, magnetite (Fe_3O_4). Because of the large quantity of the gas phases produced in these experiments, we are able to conclusively identify the gas species and quantitatively determine the content of each gas phase by GC measurements, providing details on the production and ratios of the light hydrocarbons including CH_4, C_2H_6, and C_3H_8. In Fig. 8, we summarize previous experimental studies on the synthesis of abiotic hydrocarbon in a P-T phase diagram, and compare with the experimental conditions in this study. The typical subduction geotherms are also plotted for comparison. Combining our petrological observation and experimental simulation from previous and this study, we propose a possible abiotic formation mechanism of hydrocarbon from the reduction of carbonate at high-pressure and high-temperature conditions, especially in subduction environments with water saturation as the S.W. Tianshan subduction zone (Okamoto and Maruyama, 1999).

6. CONCLUSIONS

Both field observations and laboratory experiments have provided conclusive evidence that light hydrocarbons and graphite can form from the reduction of carbonates in the presence of water at high pressure and temperature in subduction environments. The presence of oxidized iron (Fe_3O_4) and reduced carbon species in the system is documented in the field specimen and the recovered experimental charges. This redox reaction could be an important mechanism for generating hydrocarbons in the subduction zone where carbonates and water are abundant. This is further supported by thermodynamic calculations (e.g. French, 1966; Connolly, 1995 and calculations in this study) and Deep Earth Water theoretical models (Sverjensky et al., 2014). We have also demonstrated that heavier hydrocarbons such as ethane and propane, identified by GC measurements, could be synthesized at pressures as low as 1.5 GPa. The significance of finding methane-ethane inclusions in the carbonated eclogite extends to a general abiotic formation of light hydrocarbons associated with Fe-bearing carbonates and reduced fluids in subduction zone settings with low oxygen fugacity. The

high-pressure experiments coupled with Raman spectroscopic and GC measurements open new research opportunities for the detailed study of hydrocarbon formation in the deep earth under well-controlled experimental environments.

ACKNOWLEDGMENTS

This work was supported by the NSF of China (Grants 41520104004; 41502038; 41330210), and by the DREAM project of MOST, China (Grant No. 2016YFC0600408). V.S. acknowledge financial support from the Deep Carbon Observatory. We thank three anonymous reviewers, Associate Editor Dr. Weidong Song for their constructive suggestions to improve this manuscript. We also thank Haifei Zheng and Xiang Wu for their suggestions, and Guiming Shu, Qiang He and Yong Li for their technical assistance. We thank the Smithsonian Institution for providing the natural ankerite sample from Hollopatak, Hungary.

REFERENCES

Ague J. J. and Nicolescu S. (2014) Carbon dioxide released from subduction zones by fluid-mediated reactions. *Nat. Geosci.* **7**, 355–360.

Ai Y. L., Zhang L. F., Li X. P. and Qu J. F. (2006) Geochemical characteristics and tectonic implications of HP-UHP eclogites and blueschists in southwestern Tianshan, China. *Prog. Nat. Sci.* **16**, 624–632.

Alt J. C. and Teagle D. A. H. (1999) The uptake of carbon during alteration of ocean crust. *Geochim. Cosmochim. Acta* **63**, 1527–1535.

Arai S., Ishimaru S. and Mizukami T. (2012) Methane and propane micro-inclusions in olivine in titanoclinohumite-bearing dunites from the Sanbagawa high-P metamorphic belt, Japan: hydrocarbon activity in a subduction zone and Ti mobility. *Earth Planet. Sci. Lett.* **353–354**, 1–11.

Atamas N. A., Yaremko A. M., Seeger T., Leipertz A., Bienko A., Latajka Z., Ratajczak H. and Barnes A. J. (2004) A study of the Raman spectra of alkanes in the Fermi-resonance region. *J. Mol. Struct.* **708**, 189–195.

Aulbach S. and Stagno V. (2016) Evidence for a reducing Archean ambient mantle and its effects on the carbon cycle. *Geology* **44**, 751–754.

Berner R. A. (1999) A new look at the long-term carbon cycle. *GSA Today* **9**, 1–6.

Bézos A. and Humler E. (2005) The $Fe^{3+}/\Sigma Fe$ ratios of MORB glasses and their implications for mantle melting. *Geochim. Cosmochim. Acta* **69**, 711–725.

Borfecchia E., Mino L., Gianolio D., Groppo C., Malaspina N., Martinez-Criado G., Sans J. A., Poli S., Castelli D. and Lamberti C. (2012) Iron oxidation state in garnet from a subduction setting: a micro-XANES and electron microprobe ("flank method") comparative study. *J. Anal. At. Spectrom.* **27**, 1725–1733.

Brovarone A. V., Martinez I., Elmaleh A., Compagnoni R., Chaduteau C., Ferraris C. and Esteve I. (2017) Massive production of abiotic methane during subduction evidenced in metamorphosed ophicarbonates from the Italian Alps. *Nat. Commun.* **8**, 14134.

Bryndzia L. T. and Wood B. J. (1990) Oxygen thermobarometry of abyssal spinel peridotites: the redox state and C-O-H volatiles composition of the Earth's sub-oceanic upper mantle. *Am. J. Sci.* **290**, 1093–1116.

Cao Y., Song S. G., Niu Y. L., Jung H. and Jin Z. M. (2011) Variation of mineral composition, fabric and oxygen fugacity from massive to foliated eclogites during exhumation of subducted ocean crust in the North Qilian suture zone, NW China. *J. Metamorph. Geol.* **29**, 699–720.

Cartigny P. (2005) Stable isotopes and the origin of diamond. *Elements* **1**, 79–84.

Chen J. Y., Jin L. J., Dong J. P., Zheng H. F. and Liu G. Y. (2008) Methane formation from $CaCO_3$ reduction catalyzed by high pressure. *Chin. Chem. Lett.* **19**, 475–478.

Chou I. M. and Anderson A. J. (2009) Diamond dissolution and the production of methane and other carbon-bearing species in hydrothermal diamond-anvil cells. *Geochim. Cosmochim. Acta* **73**, 6360–6366.

Christie D. M., Carmichael I. S. E. and Langmuir C. H. (1986) Oxidation states of mid-ocean ridge basalt glasses. *Earth Planet. Sci. Lett.* **79**, 397–411.

Claypool G. E. and Kaplan I. R. (1974) The origin and distribution of methane in marine sediments. *Nat. Gases Mar. Sediments*, 99–139.

Connolly J. A. D. (1995) Phase diagram methods for graphitic rocks and application to the system C-O-H-FeO-TiO_2-SiO_2. *Contrib. Miner. Petrol.* **119**, 94–116.

Dasgupta R. (2013) Ingassing, storage, and outgassing of terrestrial carbon through geologic time. *Rev. Mineral. Geochem.* **75**, 183–229.

Debret B., Andreani M., Muñoz M., Bolfan-Casanova N., Carlut J., Nicollet C., Schwartz S. and Trcera N. (2014) Evolution of Fe redox state in serpentine during subduction. *Earth Planet. Sci. Lett.* **400**, 206–218.

Donohue C. L. and Essene E. J. (2000) An oxygen barometer with the assemblage garnet-epidote. *Earth Planet. Sci. Lett.* **18**, 459–472.

Duncan M. S. and Dasgupta R. (2017) Rise of Earth's atmospheric oxygen controlled by efficient subduction of organic carbon. *Nat. Geosci.* **10**, 387–392.

Etiope G. and Schoell M. (2014) Abiotic gas: atypical, but not rare. *Elements* **10**, 291–296.

Foley S. F. (2011) A reappraisal of redox melting in the Earth's mantle as a function of tectonic setting and time. *J. Petrol.* **52**, 1363–1391.

French B. M. (1966) Some geological implications of equilibrium between graphite and a C-H-O gas phase at high temperature and pressures. *Rev. Geophys* **4**, 223–253.

Frezzotti M. L., Selverstone J., Sharp Z. D. and Compagnoni R. (2011) Carbonate dissolution during subduction revealed by diamond-bearing rocks from the Alps. *Nat. Geosci.* **4**, 703–706.

Froelich P. N., Klinkhammer G. P., Berder M. L., Luedtke N. A., Heath G. R., Cullen D. and Dauphin P. (1979) Early oxidation of organic matter in pelagic sediments of the eastern equatorial Atlantic: suboxic diagenesis. *Geochim. Cosmochim. Acta* **43**, 1075–1090.

Frost B. R. (1979) Metamorphism of iron-formation parageneses in the system Fe-Si-C-O-H. *Econ. Geol.* **74**, 775–785.

Frost D. J. (2012) The carbon cycle in Earth's interior and the formation of diamonds BGI Annual Report 2012 and lists of publications 3.pp. 19–37.

Frost D. J. and McCammon C. A. (2008) The redox state of Earth's mantle. *Annu. Rev. Earth Planet. Sci.* **36**, 389–420.

Fu B., Touret J. L. R., Zheng Y.-F. and Jahn B.-M. (2003) Fluid inclusions in granulites, granulitized eclogites and garnet clinopyroxenites from the Dabie-Sulu terranes, eastern China. *Lithos* **70**, 293–319.

Gao J. and Klemd R. (2001) Primary fluids entrapped at blueschist to eclogite transition: evidence from the Tianshan meta-subduction complex in northwestern China. *Contrib. Miner. Petrol.* **142**, 1–14.

Gao J., John T., Klemd R. and Xiong X. (2007) Mobilization of Ti–Nb–Ta during subduction: evidence from rutile-bearing dehydration segregations and veins hosted in eclogite, Tianshan, NW China. *Geochim. Cosmochim. Acta* **71**, 4974–4996.

Galvez M. E., Beyssac O., Martinez I., Benzerara K., Chaduteau C., Malvoisin B. and Malavieille J. (2013) Graphite formation by carbonate reduction during subduction. *Nat. Geosci.* **6**, 473–477.

Giardini A. A. and Salotti C. A. (1969) Kinetics and relation in the calcite-hydrogen reaction and relations in the dolomite-hydrogen and siderite-hydrogen system. *Am. Mineral.* **54**, 1151–1172.

Gudmundsson G. and Wood B. J. (1995) Experimental tests of garnet peridotite oxygen barometry. *Contrib. Miner. Petrol.* **119**, 56–67.

Hacker B. R. (2003) Subduction factory 1. Theoretical mineralogy, densities, seismic wave speeds, and H_2O contents. *J. Geophys. Res.* **108**, 2029.

Herms P., John T., Bakker R. J. and Schenk V. (2012) Evidence for channelized external fluid flow and element transfer in subducting slabs (Raspas Complex, Ecuador). *Chem. Geol.* **310–311**, 79–96.

Holland T. J. B. and Powell R. (1998) An internally consistent thermodynamic data set for phases of petrological interest petrological interest. *J. Metamorph. Geol.* **16**, 309–343.

Holland T. J. B. and Powell R. (2011) An improved and extended internally consistent thermodynamic dataset for phases of petrological interest, involving a new equation of state for solids. *J. Metamorph. Geol.* **29**, 333–383.

Höfer H. E. and Brey G. P. (2007) The iron oxidation state of garnet by electron microprobe: its determination with the flank method combined with major-element analysis. *Am. Mineral.* **92**, 873–885.

Höfer H. E., Brey G. P., Schulz-Dobrick B. and Oberhänsli R. (1994) The determination of the oxidation state of iron by the electron microprobe. *Eur. J. Mineral.* **6**, 407–418.

Huang F., Daniel I., Cardon H., Montagnac G. and Sverjensky D. A. (2017) Immiscible hydrocarbon fluids in the deep carbon cycle. *Nat. Commun.* **8**, 15798.

Ickert R. B., Stachel T., Stern R. A. and Harris J. W. (2013) Diamond from recycled crustal carbon documented by coupled $\delta^{18}O$–$\delta^{13}C$ measurements of diamonds and their inclusions. *Earth Planet. Sci. Lett.* **364**, 85–97.

Isshiki M., Irifune T., Hirose K., Ono S., Ohishi Y., Watanuki T., Nishibori E., Takata M. and Sakata M. (2004) Stability of magnesite and its high-pressure form in the lowermost mantle. *Nature* **427**, 60–63.

Javoy M., Pineau F. and Allegre C. J. (1982) Carbon Geodynamic Cycle. *Nature* **300**, 171–173.

Kelemen P. B. and Manning C. E. (2015) Reevaluating carbon fluxes in subduction zones, what goes down, mostly comes up. *Proc. Natl. Acad. Sci. USA* **112**, E3997–E4006.

Kelley K. A. and Cottrell E. (2009) Water and the oxidation state of subduction zone magmas. *Science* **325**, 605–607.

Kiseeva E. S., Wood B. J., Ghosh S. and Stachel T. (2016) The pyroxenite-diamond connection. *Geochem. Perspect. Lett.* **2**, 1–9.

Kiseeva E. S., Vasiukov D. M., Wood B. J., McCammon C., Stachel T., Bykov M., Bykova E., Chumakov A., Cerantola V., Harris J. W. and Dubrovinsky L. (2018) Oxidized iron in garnets from the mantle transition zone. *Nat. Geosci.* **11**, 144–147.

Leake B. E., Woolley A. R., Arps C. E. S., Birch W. D., Gilbert M. C., Grice J. D., Hawthorne F. C., Kato A., Kisch H. J., Krivovichev V. G., Linthout K., Laird J., Mandarino J. A., Maresch W. V., Nickel E. H., Rock N. M. S., Schumacher J. C., Smith D. C., Stephenson N. C. N., Ungaretti L., Whittaker E. J. W. and Guo Y. Z. (1997) Nomenclature of amphiboles: report of the subcommittee on amphiboles of the international mineralogical association, commission on new minerals and mineral names. *Am. Mineral.* **82**, 1019–1037.

Li Y. (2016) Immiscible C-H-O fluids formed at subduction zone conditions. *Geochem. Perspect. Lett.* **3**, 12–21.

Li J. L., Klemd R., Gao J. and Meyer M. (2014) Compositional zoning in dolomite from lawsonite-bearing eclogite (SW Tianshan, China): evidence for prograde metamorphism during subduction of oceanic crust. *Am. Mineral.* **99**, 206–217.

Liu X., Chen J., Tang J., He Q., Li S., Peng F., He D., Zhang L. and Fei Y. (2012a) A large volume cubic press with a pressure-generating capability up to about 10 GPa. *High Pressure Res.: Int. J.* **32**, 239–254.

Liu X., Wang S., He Q., Chen J., Wang H., Li S., Peng F., Zhang L. and Fei Y. (2012b) Thermal elastic behavior of $CaSiO_3$-walstromite: a powder X-ray diffraction study up to 900 °C. *Am. Mineral.* **97**, 262–267.

Lin F., Bodnar R. J. and Becker S. P. (2007) Experimental determination of the Raman CH_4 symmetric stretching (ν_1) band position from 1–650 bar and 0.3–22 °C: application to fluid inclusion studies. *Geochim. Cosmochim. Acta* **71**, 3746–3756.

Lollar B. S., Westgate T. D., Ward J. A., Slater G. F. and Lacrampe-Couloume G. (2002) Abiogenic formation of alkanes in the Earth's crust as a minor source for global hydrocarbon reservoirs. *Nature* **416**, 522–524.

Lollar B. S., Lacrampe-Couloume G., Voglesonger K., Onstott T. C., Pratt L. M. and Slater G. F. (2008) Isotopic signatures of CH_4 and higher hydrocarbon gases from Precambrian Shield sites: a model for abiogenic polymerization of hydrocarbons. *Geochim. Cosmochim. Acta* **72**, 4778–4795.

Luth R. W. (1993) Diamond, eclogites and the oxidation state of the Earth's mantle. *Science* **261**, 66–68.

Luth R. W., Virgo D., Boyd F. R. and Wood B. J. (1990) Ferric iron in mantle-derived garnets: implications for thermobarometry and for the oxidation state of the mantle. *Contrib. Miner. Petrol.* **104**, 56–72.

Lü Z., Zhang L., Du J. and Bucher K. (2008) Coesite inclusions in garnet from eclogitic rocks in western Tianshan, northwest China: convincing proof of UHP metamorphism. *Am. Mineral.* **93**, 1845–1850.

Lü Z., Zhang L. F., Du J. X. and Bucher K. (2009) Petrology of coesite-bearing eclogite from Habutengsu Valley, western Tianshan, NW China and its tectonometamorphic implications. *J. Metamorph. Geol.* **27**, 773–787.

Lü Z., Zhang L., Du J., Yang X., Tian Z. and Xia B. (2012) Petrology of HP metamorphic veins in coesite-bearing eclogite from western Tianshan, China: fluid processes and elemental mobility during exhumation in a cold subduction zone. *Lithos* **136–139**, 168–186.

Lü Z., Bucher K. and Zhang L. F. (2013) Omphacite-bearing calcite marble and associated coesite-bearing pelitic schist from the meta-ophiolitic belt of Chinese western Tianshan. *J. Asian Earth Sci.* **76**, 37–47.

Malaspina N., Poli S. and Fumagalli P. (2009) The oxidation state of metasomatized mantle wedge: insights from C-O-H-bearing garnet peridotite. *J. Petrol.* **50**, 1533–1552.

Malvoisin B., Chopin C., Brunet F. and Galvez M. E. (2011) Low-temperature wollastonite formed by carbonate reduction: a marker of serpentinite redox conditions. *J. Petrol.* **53**, 159–176.

Marocchi M., Bureau H., Fiquet G. and Guyot F. (2011) In-situ monitoring of the formation of carbon compounds during the dissolution of iron(II) carbonate (siderite). *Chem. Geol.* **290**, 145–155.

Mattinson C. G., Zhang R. Y., Tsujimori T. and Liou J. G. (2004) Epidote-rich talc-kyanite-phengite eclogites, Sulu terrane, eastern China: P-T-fO_2 estimates and the significance of the epidote-talc assemblage in eclogite. *Am. Mineral.* **89**, 1772–1783.

Matveev S., Ballhaus C., Fricke K., Truchenbrodt J. and Ziegenbein D. (1997) Volatiles in the Earth's mantle: I. Synthesis of CHO fluids at 1273 K and 2.4 GPa. *Geochim. Cosmochim. Acta* **61**, 3081–3088.

McCammon C. A., Chaskar V. and Richards G. G. (1991) A technique for spatially resolved Mössbauer spectroscopy applied to quenched metallurgical slags. *Meas. Sci. Technol.* **2**, 657–662.

McCollom T. M. (2003) Formation of meteorite hydrocarbons from thermal decomposition of siderite ($FeCO_3$). *Geochim. Cosmochim. Acta* **67**, 311–317.

McDermott J. M., Seewald J. S., German C. R. and Sylva S. P. (2016) Pathways for abiotic organic synthesis at submarine hydrothermal fields. *Proc. Natl. Acad. Sci. USA* **112**, 7668–7672.

Melton C. E. and Giardini A. A. (1974) The composition and significance of gas released from natural diamonds from Africa and Brazil. *Am. Mineral.* **59**, 775–782.

Milesi V., Guyot F., Brunet F., Richard L., Recham N., Benedetti M., Dairou J. and Prinzhofer A. (2015) Formation of CO_2, H_2 and condensed carbon from siderite dissolution in the 200–300 °C range and at 50 MPa. *Geochim. Cosmochim. Acta* **154**, 201–211.

Morimoto N., Fabries J., Ferguson A. K., Ginzburg I. V., Ross M., Seifert F. A., Zussman J., Aoki K. and Gottardi G. (1988) Nomenclature of pyroxenes. *Am. Mineral.* **73**, 1123–1133.

Okamoto K. and Maruyama S. (1999) The high-pressure synthesis of lawsonite in the MORB + H_2O system. *Am. Mineral.* **84**, 362–373.

Pan C., Yu L., Liu J. and Fu J. (2006) Chemical and carbon isotopic fractionations of gaseous hydrocarbons during abiogenic oxidation. *Earth Planet. Sci. Lett.* **246**, 70–89.

Parkinson I. J. and Arculus R. J. (1999) The redox state of subduction zones: insights from arc-peridotites. *Chem. Geol.* **160**, 409–423.

Plank T. (2014) The chemical composition of subducting sediments. Treatise on. *Geochemistry* **4**, 607–629.

Poli S. (2015) Carbon mobilized at shallow depths in subduction zones by carbonatitic liquids. *Nat. Geosci.* **8**, 633–636.

Poli S., Franzolin E., Fumagalli P. and Crottini A. (2009) The transport of carbon and hydrogen in subducted oceanic crust: an experimental study to 5 GPa. *Earth Planet. Sci. Lett.* **278**, 350–360.

Scott H. P., Hemley R. J., Mao H.-K., Herschbach D. R., Fried L. E., Howard W. M. and Bastea S. (2004) Generation of methane in the Earth's mantle: In situ high pressure-temperature measurements of carbonate reduction. *Proc. Natl. Acad. Sci. USA* **101**, 14023–14026.

Shen T., Hermann J., Zhang L., Lü Z., Padrón-Navarta J. A., Xia B. and Bader T. (2015) UHP metamorphism documented in ti-chondrodite- and ti-clinohumite-bearing serpentinized ultramafic rocks from chinese southwestern tianshan. *J. Petrol.* **56**, 1425–1458.

Shi G. U., Tropper P., Cui W., Tan J. and Wang C. (2005) Methane (CH_4)-bearing fluid inclusions in the Myanmar jadeitite. *Geochem. J.* **39**, 503–516.

Sleep N. H. and Zahnle K. (2001) Carbon dioxide cycling and implications for climate on ancient Earth. *J. Geophys. Res. Planets* **106**, 1373–1399.

Song S., Su L., Niu Y., Lai Y. and Zhang L. (2009) CH_4 inclusions in orogenic harzburgite: evidence for reduced slab fluids and implication for redox melting in mantle wedge. *Geochim. Cosmochim. Acta* **73**, 1737–1754.

Stagno V., Ojwang D. O., McCammon C. A. and Frost D. J. (2013) The oxidation state of the mantle and the extraction of carbon from Earth's interior. *Nature* **493**, 84–88.

Stagno V., Frost D. J., McCammon C. A., Mohseni H. and Fei Y. (2015) The oxygen fugacity at which graphite or diamond forms from carbonate-bearing melts in eclogitic rocks. *Contrib. Miner. Petrol.* **169**. https://doi.org/10.1007/s00410-015-1111-1.

Staudigel H., Hart S. R., Schmincke H. U. and Smith B. M. (1989) Cretaceous ocean crust at DSDP sites 417 and 418: carbon uptake from weathering versus loss by magmatic outgassing. *Geochim. Cosmochim. Acta* **53**, 3091–3094.

Sverjensky D. A., Stagno V. and Huang F. (2014) Important role for organic carbon in subduction-zone fluids in the deep carbon cycle. *Nat. Geosci.* **7**, 909–913.

Tao R. B., Fei Y. W. and Zhang L. F. (2013) Experimental determination of siderite stability at high pressure. *Am. Mineral.* **98**, 1565–1572.

Tao R., Zhang L., Fei Y. and Liu Q. (2014) The effect of Fe on the stability of dolomite at high pressure: experimental study and petrological observation in eclogite from southwestern Tianshan, China. *Geochim. Cosmochim. Acta* **143**, 253–267.

Tao R., Zhang L., Liu X., Bader T. and Fei Y. (2017a) Phase relations and formation of K-bearing Al-10 Å phase in the MORB + H_2O system: implications for H_2O- and K-cycles in subduction zones. *Am. Mineral.* **102**, 1922–1933.

Tao R., Zhang L., Stagno V., Chu X. and Liu X. (2017b) High-pressure experimental verification of rutile-ilmenite oxybarometer: implications for the redox state of the subduction zone. *Sci. China Earth Sci.*

Tao R., Zhang L., Li S., Zhu J. and Ke S. (2018a) Significant contrast in the Mg-C-O isotopes of carbonate between carbonated eclogite and marble from the S.W. Tianshan UHP subduction zone: evidence for two sources of recycled carbon. *Chem. Geol.* **483**, 65–77.

Tao R., Fei Y., Bullock E. S., Xu C. and Zhang L. (2018b) Experimental investigation of Fe^{3+} - rich majoritic garnet and its effect on majorite geobarometer. *Geochim. Cosmochim. Acta* **225**, 1–16.

Tatsumi Y. (2005) The subduction factory: how it operates in the evolving Earth. *GSA Today* **15**, 4–10.

Thomson A. R., Kohn S. C., Bulanova G. P., Smith C. B., Araujo D., EIMF and Walter M. J. (2014) Origin of sub-lithospheric diamonds from the Juina-5 kimberlite (Brazil): constraints from carbon isotopes and inclusion compositions. *Contrib. Miner. Petrol.* **168**, 1081.

Tian Z. L. and Wei C. J. (2012) Metamorphism of ultrahigh-pressure eclogites from the Kebuerte Valley, South Tianshan, NW China: phase equilibria and P-T path. *J. Metamorph. Geol.* **31**, 281–300.

White R. W., Powell R. and Phillips G. N. (2003) A mineral equilibria study of the hydrothermal alteration in mafic greenschist facies rocks at Kalgoorlie, Western Australia. *J. Metamorphic Geol.* **21**, 455–468.

Wood B. J. and Virgo D. (1989) Upper mantle oxidation state: ferric iron contents of lherzolite spinels by ^{57}Fe Mössbauer spectroscopy and resultant oxygen fugacities. *Geochim. Cosmochim. Acta* **53**, 1277–1291.

Woodland A. B. and O'Neill H. S. C. (1993) Synthesis and stability of $Fe_3^{2+}Fe_2^{3+}Si_3O_{12}$ garnet and phase relations with $Fe_3Al_2Si_3O_{12}$ - $Fe_3^{2+}Fe_2^{3+}Si_3O_{12}$ solutions. *Am. Mineral.* **78**, 1002–1005.

Xiao Y., Lavis S., Niu Y., Pearce J. A., Li H., Wang H. and Davidson J. (2012) Trace-element transport during subduction-zone ultrahigh-pressure metamorphism: Evidence from western Tianshan, China. *Geol. Soc. Am. Bull.* **124**, 1113–1129.

Xu C., Kynický J. i., Tao R., Liu X., Zhang L., Pohanka M., Song W. and Fei Y. (2017) Recovery of an oxidized majorite inclusion from Earth's deep asthenosphere. *Sci. Adv.* **3**, 1–7.

Yang X., Zhang L., Tian Z. and Bader T. (2013) Petrology and U-Pb zircon dating of coesite-bearing metapelite from the Kebuerte Valley, western Tianshan, China. *J. Asian Earth Sci.* **70–71**, 295–307.

Zhang C. and Duan Z. (2009) A model for C-O-H fluid in the Earth's mantle. *Geochim. Cosmochim. Acta* **73**, 2089–2102.

Zhang L., Ellis D. and Jiang W. (2002a) Ultrahigh-pressure metamorphism in western Tianshan, China: Part I. Evidence from inclusions of coesite pseudomorphs in garnet and from quartz exsolution lamellae in omphacite in eclogites. *Am. Mineral.* **87**, 853–860.

Zhang L., Ellis D., Williams S. and Jiang W. (2002b) Ultra-high-pressure metamorphism in western Tianshan, China Part II. Evidence from magnesite in eclogite. *Am. Mineral.* **87**, 861–866.

Zhang L., Ai Y. and Song S. (2007) A brief review of UHP meta-ophiolitie rocks, southwestern Tianshan, Western China. *Int. Geol. Rev.* **49**, 811–823.

Associate editor: Weidong Sun